Delft University of Technology

Microstructure evolution and micromechanical behavior of solvent-modified Cu–Ag composite sintered joints for power electronics packaging at high temperatures

Wang, Xinyue; Chen, Haixue; Yang, Zhoudong; Liu, Wenting; Zeng, Zejun; Zhang, Guoqi; Zhang, Jing; Fan, Jiajie; Liu, Pan

Important note
To cite this publication, please use the final published version (if applicable).
Please check the document version above.

Microstructure evolution and micromechanical behavior of solvent-modified Cu–Ag composite sintered joints for power electronics packaging at high temperatures

Xinyue Wang [a], Haixue Chen [a], Zhoudong Yang [a], Wenting Liu [a], Zejun Zeng [a], Guoqi Zhang [b], Jing Zhang [c], Jiajie Fan [a], Pan Liu [a,d,*]

[a] *Academy for Engineering & Technology, Fudan University, Shanghai, 200433, China*
[b] *Department of Microelectronics, Delft University of Technology, 2628 CD, Delft, the Netherlands*
[c] *Heraeus Materials Technology Shanghai Ltd., Shanghai, 201108, China*
[d] *Research Institute of Fudan University in Ningbo, Zhejiang Province, 315336, China*

ARTICLE INFO

ABSTRACT

With the increased deployment of power modules in demanding conditions, sintering materials, especially composite sintering materials, have raised growing interest due to their cost-effectiveness and suitability. Therefore, this study explores the viability of Cu–Ag composite sintering material, focusing on solvent influence through microstructure and mechanical behavior analysis. Micron-sized particle-based Cu–Ag composite pastes were designed and compared using eight solvents (four epoxy-free and four epoxy-added) based on fluidity and thermal stability. The sintered joints' performance, assessed through shear strength analysis, showed comparable values to pure silver sintering for both epoxy-free and epoxy-added samples. Optimized samples from each solvent system underwent reliability analysis, demonstrating that Cu–Ag joints with epoxy resin exhibited significantly higher shear strength after high-temperature storage and thermal cycling tests. Micromorphology and elemental composition analysis revealed differences in aging mechanisms, primarily attributed to variations in porosity due to oxide formation and pore filling by epoxy resin under different solvent systems. Further nanoindentation characterization of micromechanical properties, including hardness, modulus, and creep properties, during high-temperature aging, established constitutive models for insights into reliability evolution. In conclusion, the optimized epoxy-added Cu–Ag sintered joints proposed in this study demonstrated exceptional reliability and acceptable micromechanical properties, presenting a promising option for high-temperature power packaging.

1. Introduction

As the demand for wide band-gap (WBG) electronic components continues to increase, the need for advanced packaging materials and manufacturing techniques capable of withstanding extreme thermal and mechanical conditions in power electronics applications is becoming more pronounced [1–3]. Die-attach materials, among packaging materials for power electronics, play a crucial role in ensuring the efficient and reliable operation of electronic devices under harsh conditions [4, 5]. However, traditional lead-free solder material faces limitations in terms of high operating temperatures and mechanical performance, which is unsuitable for WBG chips [6]. As a result, recent developments

have given rise to low-temperature sintering technologies, specifically silver sintering and copper sintering [4,7–9].

Sintering joints offer commendable electrical and thermal conductivity while operating at reduced processing temperatures [10]. However, silver's high cost and susceptibility to electromigration, coupled with copper's tendencies toward agglomeration and oxidation, resulting in elevated sintering temperatures, pose inherent limitations [8]. To overcome these challenges, researchers have explored Cu–Ag composite sintering pastes that blend the advantages of silver and copper, avoiding the formation of brittle intermetallic compounds (IMC) [11–13]. There are mainly two strategies for Cu–Ag sintering composites. One is to simply mix Cu and Ag particles [14]. Studies by Li et al. [15] on Cu–Ag

* Corresponding author. Academy for Engineering & Technology, Fudan University, Shanghai, 200433, China.
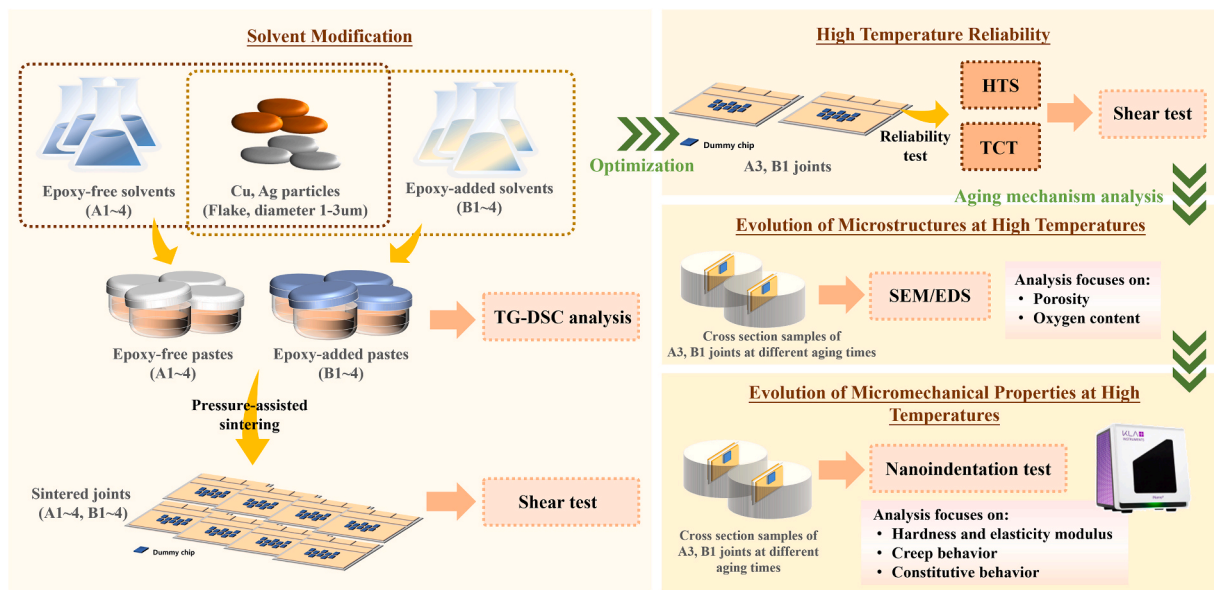*E-mail address:* panliu@fudan.edu.cn (P. Liu).

Fig. 1. Schematic diagram of the research technology roadmap of this work.

paste with 60 nm particles, yielding 25.41 MPa shear strength, and by Kim et al. [16] on Cu–Ag paste with 50 nm particles achieving 40.5 MPa shear strength on copper substrates, showcase robust joint strength attributed to the nanosize effect. Another strategy is to apply Ag around Cu, with core-shell structures (Cu@Ag) [17–19]. C.H. Lee et al. [20] synthesized Cu@Ag particles with diameters of 200 or 350 nm, demonstrating shear strengths of up to 18.0 MPa. J.H. Lee et al. [21] reported a bonding strength of approximately 24 MPa using 350 nm Cu@Ag particles. Yet, the cost-intensive nanocore-shell structure has prompted a shift towards the cost-effective alternative of directly mixing copper and silver. However, most research mentioned above is based on nanoscale metal particles. The potential biological toxicity of nanomaterials warrants consideration, limiting exploration into high-strength nano-sized Cu–Ag composite sintered materials for die-attach [22]. Hence, there is a crucial need to investigate suitable organic solvents to enhance micron-sized sintering quality.

Moreover, despite the exceptional performance of sintered joints in normal operating conditions, their behavior under prolonged exposure to high temperatures is a crucial consideration, especially in challenging environments [23]. The existing research primarily focuses on the macroscopic evolution of mechanical properties, particularly shear strength [5,23]. However, there is a lack of investigation into micromechanical parameters such as elastic modulus and hardness. Such lack of examination is probably attributed to the difficulties of sample preparation since conventional dog bone rod test specimens are difficult to establish for sintered Ag and Cu materials [24–26]. In recent years, the emergence of nanoindentation analysis has provided a powerful and localized method for the comprehensive evaluation of mechanical properties at the nanoscale [26–28]. This technique provides valuable data regarding crucial parameters like hardness, elastic modulus, and other mechanical characteristics [29,30]. Importantly, the technique's enhanced spatial resolution makes it highly suitable for a detailed examination of sintering materials, enabling researchers to investigate specific regions of interest within the intricate packing system [28]. Chen et al. [31] evaluated the microscale mechanical properties of sintered Ag consisting of various shapes using a focused ion beam process and a nano-indentation system. They suggested that the size and shape of the utilized Ag particles significantly influence its fracture behavior and mechanical properties. T. Ishizaki et al. [32] conducted power and thermal cycle tests on the sintered Cu joints between Al_2O_3 heater chips and heatsinks. The Young's module of the sintered Cu was evaluated by nanoindentation tests, indicating that the sintered structures were strengthened at higher temperatures. However, there is a lack of research on the micromechanical properties of Cu–Ag composited sintered joints and their evolution under high temperature aging, especially on the creep behavior and elastoplastic constitutive behavior.

Therefore, this work focused on micron-size Cu–Ag composite sintering material through solvent modification while achieving low cost, high reliability, and sufficient mechanical properties. The research technical route of this work was shown in Fig. 1. Firstly, eight kinds of micron-scale Cu–Ag composite sintering pastes belonging to two solvent systems including epoxy-free and epoxy-added were designed and fabricated. The contributions of solvent optimization were explored by analyzing TG-DSC and shear strength. Then, reliability analysis
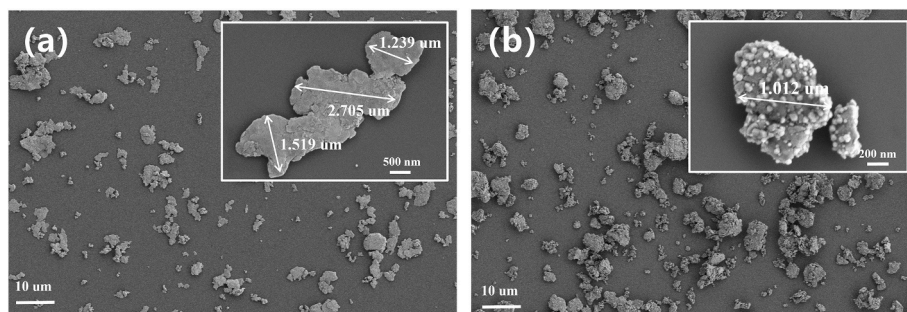

Fig. 2. Scanning electron microscope (SEM) photos of (a)silver and (b)copper particles.

Table 1
Composition and viscosity of the designed pastes.

Paste	Particles (wt%)	Solvent (wt%)					Viscosity (Pa.s)
	Cu–Ag	T	PEG	SG	YDS	NS	
A1	85	15	–	–	–	–	4.0
A2	85	–	–	15	–	–	10.5
A3	85	5	10	–	–	–	24.1
A4	85	3	12	–	–	–	30.3
B1	85	–	–	10	5	–	55.7
B2	85	–	–	5	10	–	65.5
B3	85	–	–	10	–	5	72.0
B4	85	–	–	5	–	10	83.1

including high-temperature storage and thermal cycling tests was conducted on the optimized samples for each solvent system. Subsequently, micromorphology and elemental composition analyses were conducted on two groups of joints to unveil the aging mechanism during the high-temperature process. Furthermore, the micromechanical properties, such as hardness, modulus, and creep properties of the joint samples during high-temperature aging were investigated through the nano-indentation method. Constitutive models for both materials were applied through the finite element method to gain insights into the evolution of reliability. The findings of this study are expected to substantially contribute to the understanding of the high-temperature aging behavior of Cu–Ag composite sintered materials, thereby facilitating the development of robust and reliable materials for next-generation technologies.

2. Materials and experiments

2.1. Preparation and characterization of sintering pastes

The micron-scale flake copper and silver particles applied in this work were produced by Guangzhou Hongwu Material Technology, with particle sizes round 1–3 μm (Fig. 2).

The organic solvent selected in this work included terpineol (T) and compound thinner (SG) from Heraeus GmbH, polyethylene glycol (PEG) from Shanghai Aladdin Biochemical Technology., bisphenol A epoxy resin (YD) from KUKDO Chemical (Kunshan), phenol novolac epoxy resin (N) from Nantong Xingchen Synthetic Materials, curing agent (methyl-tetrahydro phthalic anhydride) and accelerator (2-Ethyl-4-methylimidazole) for epoxy form Jiaxing Nanyang Wanshixing Chemical. The mass ratio of resin, curing agent, and accelerator in the two epoxy resin systems (YDS, NS) was 10:9:0.9. The components of the designed 8 groups of pastes were shown in Table 1. Pastes A1~A4 contained different solvents without epoxy, while pastes B1~B4 included different epoxy-based solvents.

2.2. Preparation and characterization of sintered joints

A schematic of the sintering process was shown in Fig. 3. Firstly, copper and silver particles were mixed in a mass ratio of 1:1. Next, the powders were blended with organic solvent in a mass ratio of 85:15. A three-roll machine and agate grinder were employed. Then, the stirred

sintering paste was mixed at 1000 rpm for 3 min in a planetary mixer (THINKY ARE-310). After that, the pastes were stenciled onto the direct bonding copper substrate (DBC) by DEK NeoHorizon 03iX, and pre-dried in the BINDER M115 nitrogen oven. In the printing process, the printing parameters, including printing speed, squeegee pressure, demolding speed, and the print gap on the screen printing machine, were refined to enhance the quality of deposition. These optimizations were implemented to ensure consistent pattern fidelity and deposition uniformity for all pastes. Tresky T-3002 was utilized to mount the silver-plated silicon dummy chips ($2 \times 2 \times 0.25$ mm). Finally, the joints were sintered in the Boschman Sinterstar Innovate-F-XL under the pressure of 20 MPa for 10 min at 250 °C in nitrogen atmosphere. In addition, a similar process was used to prepare cylinder-shape test samples for electrical conductivity measurements [33]. A four-probe tester (RTS-8) was utilized to analyze electrical conductivity at a temperature of (25 ± 5)°C and 65%RH.

When dealing with solvents and pastes, it is crucial to determine the pre-drying temperature and time by analyzing the thermogravimetric curve obtained from the SDT-Q600 thermogravimetric analyzer (TA Instruments, USA). The heating rate was set at 10 °C/min, starting from room temperature and going up to 400 °C, all while under N_2 protection. The flow rate of N_2 was consistently maintained at 100 ml/min. To assess the printing performance, the flowability of the slurry was evaluated using an Anton Paar MCR 102 rheometer. The rheological measurements employed a cone-plate system, consisting of a 2° conical rotor with a diameter of 25 mm. The experiment began with a 3-min preliminary rest period, followed by a gradual increase in shear rate from 0 to 15 s^{-1} over a span of 3 min. Stress values were recorded every 6 s during this period. Subsequently, the shear rate was further increased from 16 to 35 s^{-1} over 3 min, with stress measurements taken every 3.6 s. The resulting data points were utilized to plot a shear stress-shear rate curve. The viscosity (η) was calculated using the formula :

$$\eta = \frac{\tau}{\dot{\gamma}} \tag{1}$$

where η represents the viscosity in Pa·s, τ denotes the shear stress in Pa, and $\dot{\gamma}$ represents the shear rate in s^{-1}. In this work, the viscosity at 10 s^{-1} was chosen for comparison purposes. To minimize the influence of solvent evaporation on viscosity, all experiments were conducted at a controlled temperature of 25.0 ± 0.3 °C and were performed expeditiously. This approach ensured minimal solvent loss during the measurements [34].

As for the sintered joints, shear strength was measured using a push-pull tester (Dage-4000) with a shear speed of 0.3 mm/s and a shear height of 50 μm. In order to assess the durability of the joints, a high-temperature aging test was conducted in a blast oven (DHG-9035 A) set at 250 °C for a duration of 400 h. Furthermore, a thermal cycling test was performed in a thermal shock chamber (VT3-7006S2), subjecting the joints to a temperature range of −55 to 150 °C with 2 cycles per hour for a total of 450 cycles. The independently performed high-temperature aging test and thermal cycling test were both conducted on the same batch of samples.
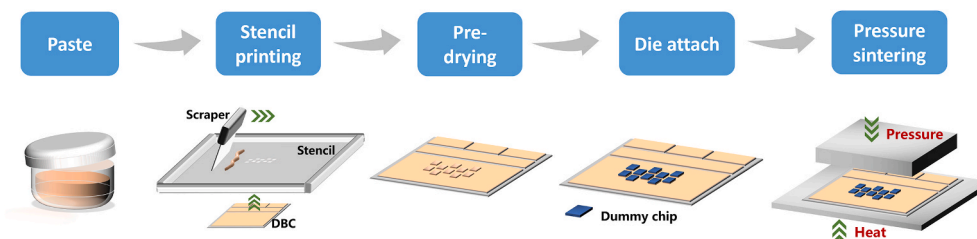

Fig. 3. Schematic of pressure-assisted sintering process.

2.3. Microstructural analysis

In order to characterize the microstructure of the sintered interconnected structure, the LaboForce-100 model grinding machine produced by the Danish company Struers was utilized. Firstly, the substrate was cut into a cross-section near the chip and placed in a mold. Then, the bisphenol A-type epoxy resin and curing agent were carefully mixed in the prescribed ratio to ensure a uniform mixture. Afterwards, a vacuum macerator was applied to remove any remaining air. The resulting compound was then injected into the mold for further solidification. The cross-sectional sample was polished with SiC sandpaper with grit sizes of 500# and 1200# on the sample grinding machine in the next step. Finally, the prepared sample was polished with a diamond spray polishing agent until no visible scratches were observed under optical microscopy, indicating the completion of the sample preparation process. After preparing such samples, their microstructure was observed by scanning electron microscopy (SEM, Gemini 300) equipped with energy-dispersed spectrometry (EDS). X-ray Photoelectron Spectroscopy (XPS, Thermo Fischer, ESCALAB Xi+) equipped with an Al K_α excitation source ($h\nu = 1486.6$ eV) was applied to study the chemical state of Cu and Ag elements of the sintered samples.

2.4. Nanoindentation measurement

Nanoindentation analysis offers a powerful and localized approach to assess mechanical properties at the nanoscale. In this work, a commercial nanoindentation apparatus iNano from KLA company with a standard diamond berkovich indenter was utilized.

2.4.1. Introduction of nanoindentation

Fig. 4(a) presented a schematic diagram of the nanoindentation test. In this process, a sharp indenter is precisely pressed into the material surface, generating a load-depth (*P-h*) curve, as shown in Fig.4(b). The applied force is continuously increased and then reduced, allowing for

the measurement of the material's response to deformation. This data is analyzed to provide valuable insights into the material's mechanical behavior on a microscopic level. Combined with the Oliver-Pharr model, a well-established method for determining hardness and modulus from indentation experiments, key parameters, including hardness (*H*) and reduced Young's Modulus (E_r) can be calculated [35].

$$\sigma = H = \frac{P_{\max}}{A_c} \tag{2}$$

$$E_r = \frac{S\sqrt{\pi}}{2\beta\sqrt{A_c}} \tag{3}$$

where *S* is contact stiffness defined as the slop of the initial unloading stage of the *P-h* curve. β is a constant related to the shape of the indenter (for a diamond berkovich indenter $\beta = 1.034$). A_c is the projected area related to the contact depth (h_c), which was expressed as :

$$A_c = 24.56h_c \tag{4}$$

Moreover, the value of E_r is determined by the elastic modulus and Poisson's ratio of the pressed sample and the indenter. Hence, E_r can be obtained by solving the following equation (5):

$$\frac{1}{E_r} = \frac{1-\nu^2}{E} + \frac{1-\nu_i^2}{E_i} \tag{5}$$

where E_i ($E_i = 1140$ GPa) and ν_i ($\nu_i = 0.07$) are the Young's modulus and Poisson's ratio of the diamond indenter, respectively. *E* and ν are the Young's modulus and Poisson's ratio of the test samples, respectively [36].

2.4.2. Creep analysis

Creep analysis in nanoindentation testing offers valuable insights into the time-dependent deformation behavior of materials at the nanoscale. The resulting creep behavior is characterized by the indentation depth evolution over time. Creep curves illustrated the time-
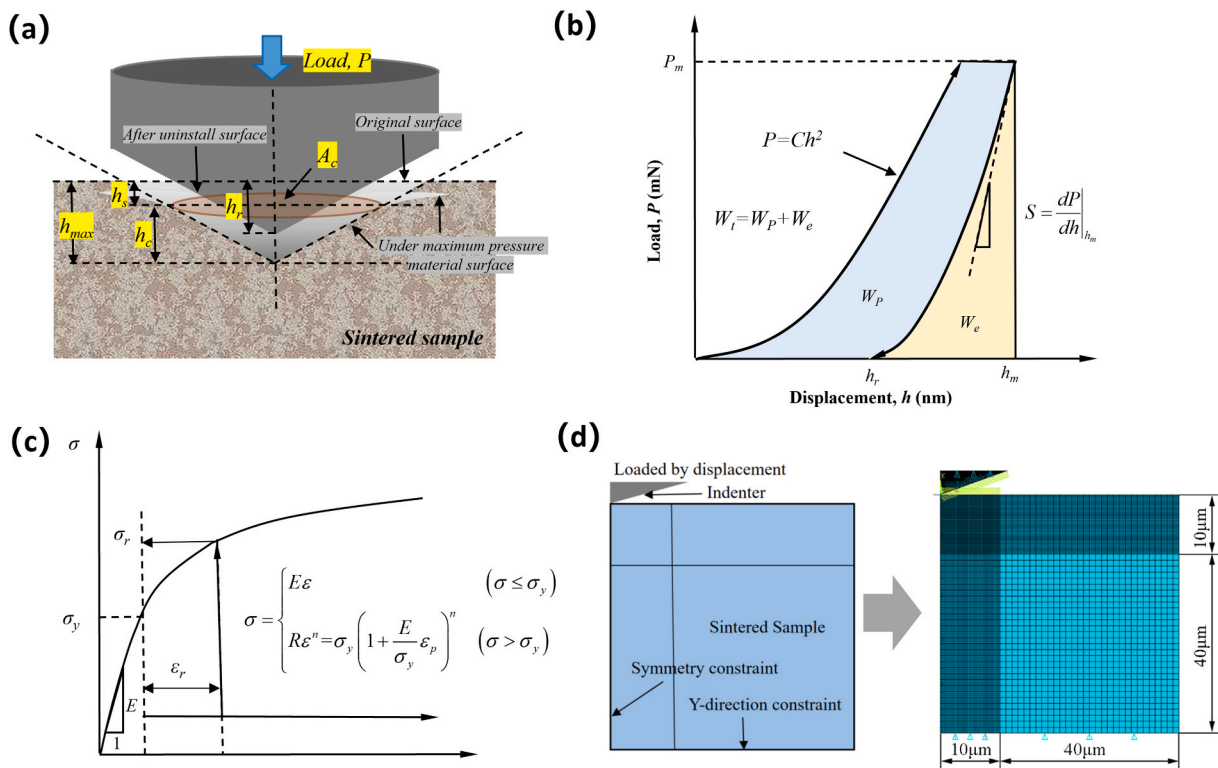

Fig. 4. (a) Schematic of a nanoindenter. (b) Schematic of a typical nanpindentation curve. (c) Power-law constitutive model curve of metallic material elastic-plastic behavior. (d) FEM model of the nanoindentation test.
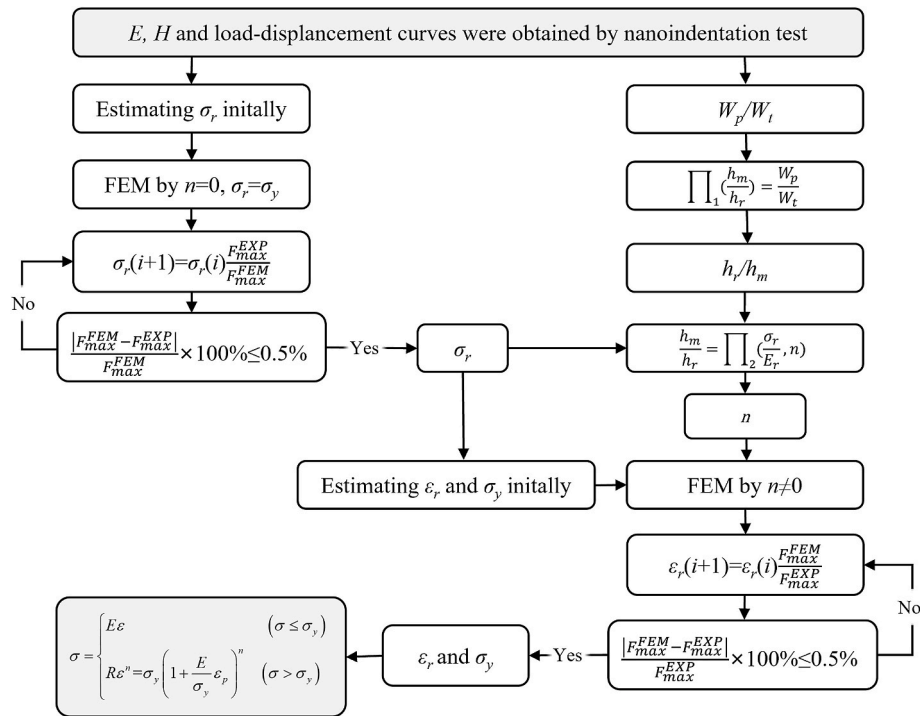
Fig. 5. Flow chart of inversion analysis.

dependent deformation, and typically exhibit three stages: primary, secondary, and tertiary creep. During the primary stage, initial deformation occurs as the material adjusts to the applied load. The secondary stage demonstrates a relatively constant strain rate, while the tertiary stage displays accelerated creep, ultimately leading to material failure which is difficult to observe in the nanoindentation test. A notable distinction in the analysis of mechanical properties and creep properties lies in the duration of the holding stage. In this study, the holding time for testing the creep behavior of the samples was set at 300 s, based on previous research.

The creep strain rate sensitivity index (m) is determined by analyzing the gradient of the creep curve during the secondary stage, wherein deformation remains relatively constant [37]. A decreased sensitivity index signifies a heightened resistance to creep deformation. The power-law relationship below is commonly used to describe the behavior of steady-state creep.

$$\dot{\varepsilon} = C\sigma^n \tag{6}$$

where C is the proportionality constant related to the material. $\dot{\varepsilon}$ and σ can be expressed as the following Eqs. (7) and (8) for the nanoindentation experiments under Berkovich indenter [38].

$$\dot{\varepsilon} = \frac{1}{h}\frac{dh}{dt} \tag{7}$$

$$\sigma = \frac{P}{24.56h^2} \tag{8}$$

where the variables h and t represent the instantaneous indentation depth and the indentation time, respectively. P represents the instantaneous applied indentation load.

Equation (6) can be rewritten as follows:

$$\frac{1}{h}\frac{dh}{dt} = C\left(\frac{P}{24.56h^2}\right)^n \tag{9}$$

Consequently, the value of m is the reciprocal of n, calculated by the following formula [39,40].

$$m = \frac{1}{n} = \frac{\partial\ln\sigma}{\partial\ln\dot{\varepsilon}} = \frac{\partial\ln\left(\frac{P}{24.56h^2}\right)}{\partial\ln\left(\frac{1}{h}\frac{dh}{dt}\right)} \tag{10}$$

2.4.3. FEM simulation inversion analysis

For the nanoindentation experiment, during the loading stage, when using the Berkovich indenter, the relationship between load and displacement satisfies the Kick model, describes as follows :

$$P = \alpha h^2 \tag{11}$$

In the formula, P is the loading load, h is the indentation depth, and α is a constant, which is related to the elastic properties of the substrate [41].

Besides, the total work (W_t) during the loading phase can be determined by adding the elastic work (W_e) and plastic work (W_p) together, as shown in Equation (12).

$$W_t = W_e + W_p \tag{12}$$

As depicted in Fig. 4(c), the stress-strain relationship of metal materials is typically depicted by the power-law strengthening model described as:

$$\sigma = \begin{cases} E\varepsilon, & \sigma \leq \sigma_y \\ R\varepsilon^n = \sigma_y\left(1 + \frac{E}{\sigma_y}\varepsilon_p\right), & \sigma > \sigma_y \end{cases} \tag{13}$$

where E is the Young's Modulus of the samples, R is the strength coefficient, n is the strain hardening index ($n = 0\sim0.5$ for metallic materials), ε_p is the generated plastic strain and σ_y is the initial yield strength [42].

As shown in Fig. 4(d), a 2D model based on the finite element method (FEM) was established in ANSYS software to simulate the nanoindentation test process. Specifically, the ANSYS Parametric Design Language (APDL) module was employed in this simulation due to its advanced capabilities in modeling complex material behavior and accurately simulating mechanical responses under nanoindentation
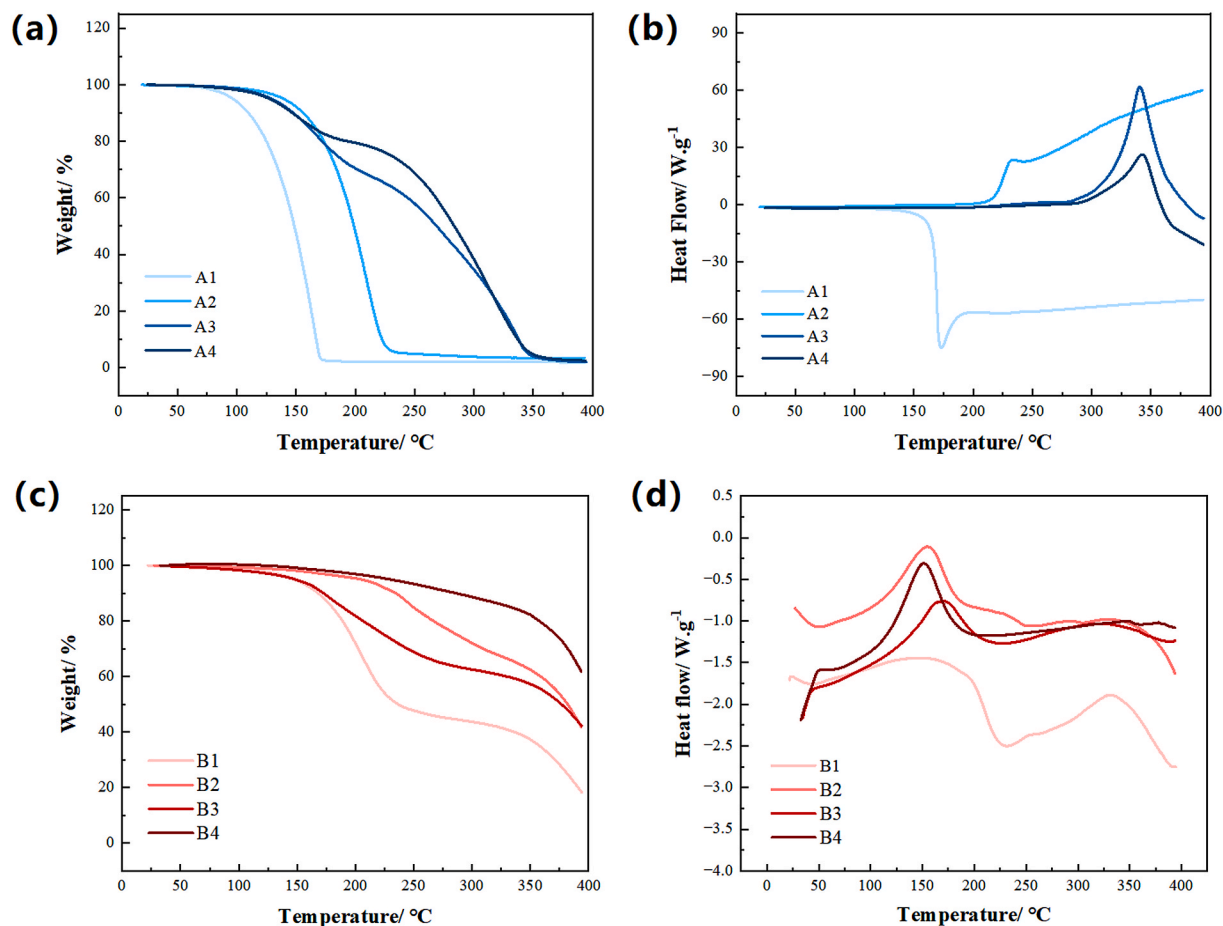
Fig. 6. (a), (b)TG-DSC results of samples A1~A4. (c), (d)TG-DSC results of samples B1~B4.

conditions. In the application of APDL, the 2D element type, PLANE182, was utilized to precisely determine characteristic stresses using bilinear isotropic hardening (BISO) and characteristic strains using multilinear isotropic hardening (MISO). The FEM model of the sintered material part (measuring 50 μm × 50 μm) was divided into four sections in order to follow Saint-Venant's principle and improve the accuracy of the mesh. Throughout the simulation, the time unit was expressed in seconds (s), the force unit in millinewtons (mN), and the units for elastic modulus and stress were megapascals (MPa). In the FEM modeling, in order to simplify the model and improve the calculation speed, it is simplified into a cone with a half-cone angle of 70.3°. Since the indenter has axial symmetry, the three-dimensional model can be simplified into a two-dimensional axisymmetric model without significant impact on the simulation results [43,44].

In this study, the method of continuous stiffness measurement (CSM) was employed to establish the elastic-plastic constitutive model of the sintered Cu–Ag composite material through the process of inversion calculation, as the flow chart depicted in Fig. 5. The CSM method allows for the continuous assessment of stiffness during loading, taking into account any changes in stress under a constant load. This technique is particularly useful in accurately capturing the material's true response and eliminating potential artifacts caused by the indentation size effect (ISE). During the CSM experiment, a loading strain rate of 0.05 s^{-1} and a maximum displacement of 1000 nm were utilized.

3. Results and discussion

3.1. Solvent modification

The organic component plays an important role in the paste as it acts as a carrier for metal particles, providing moderate fluidity before stencil printing. Solvents are also important for preventing agglomeration before sintering and achieving a low decomposition temperature with a proper decomposition rate during sintering to minimize voids and residues, particularly for micron-scale sinter pastes. In this study, viscosity analysis, thermogravimetric analysis, differential scanning calorimetry tests (TG-DSC), and shear tests were conducted to analyze the potential for future high-temperature power electronics applications.

For alcohol-based solvents (Group A), viscosity analysis of the alcohol-based pastes A1 and A2 (4.0 and 10.5 Pa s, respectively) indicated that one-component solvents were too diluted and not conducive to the printing process. Therefore, PEG was chosen to improve the viscosity of A3 and A4, resulting in viscosities of 24.1 and 30.3 Pa s, respectively. As shown in Fig. 6(a), (b), the TG curves revealed that all two-component solvent systems exhibited two stages. For the alcohol-based solvents A3 and A4, the low-boiling T component volatilized and decomposed before 200 °C, while high-boiling PEG decomposed after 200 °C.

For epoxy based solvents (Group B), epoxy markedly increased the viscosity of the solvent system due to its intrinsic properties, with NS exhibiting higher viscosity than YDS. The viscosity of pastes B1~B4 were 55.7, 65.5, 72.0, and 83.1 Pa s, respectively, which was more than double that of the alcohol-based pastes. For the epoxy-based systems (B1 and B2), there were generally the rapid volatilization and decomposition of the low-boiling component SG before 250 °C and the curing of epoxy, as shown in Fig. 6(c), (d). The epoxy solvents decomposed gradually when the temperature exceeded 350 °C. Besides, it showed that solvents with the same content of NS decomposed slower than YDS. More importantly, the results demonstrated that the epoxy-based pastes had relatively higher mass residues than the alcohol-based samples at
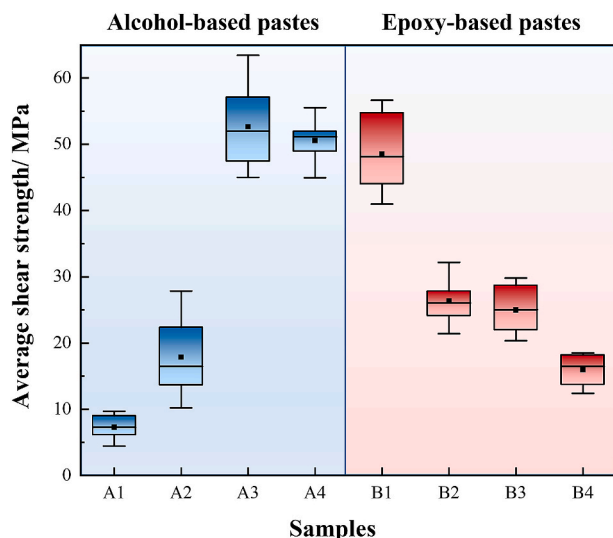
Fig. 7. Average shear strength of sintered samples.

250 °C.

Based on the thermal analysis shown in the TG-DSC results and supported by practical experience, heating processes (including pre-drying in a nitrogen oven and pre-heating in the sintering furnace protected by nitrogen) were established to optimize the sintering process for each group. The temperatures were determined by the TG-DSA tests where the speed of solvent evaporation accelerated. For the Group A samples, the pre-drying process was established at 140 °C for 20 min and the pre-heating phase at 175 °C for 3 min. While for the Group B samples, the pre-drying process was set at 90 °C for 15 min, followed by the pre-heating at 110 °C for 5 min. The determination of these specific processes aimed to optimize solvent evaporation without reaching the boiling points of organic compounds, thereby avoiding rapid solvent loss and potential defects in paste consistency and microstructure.

The performance of the joints after sintering was influenced by the presence of organic residues. The shear strength of the sintered joints prepared by the pastes at 250 °C and 20 MPa pressure-assisted sintering for 10 min was illustrated in Fig. 7. The results demonstrated that pastes A3 and B1 exhibited superior performance, achieving shear strengths of 51.70 and 48.54 MPa, respectively. Consequently, these two pastes were selected for subsequent reliability testing and analysis. Additionally, it was observed that two-component solvents outperformed single-component alcohol-based solvents. This is due to the presence of PEG,

which enhances sintered samples' shear strength through its steric hindrance and polar functional groups that form a reducible protective film on metal surfaces, promoting interparticle bonding and interface stabilization [45–47]. Furthermore, in the case of epoxy-based solvents, the incorporation of YDS enhanced the shear strength during sintering.

The cross-sections of the preferred A3 and B1 joints were observed using SEM for microstructure analysis to further investigate the difference in the bonding mechanism between the two groups of joint samples. Fig. 8 illustrated the microstructural differences between samples A3 and B1. The presence of uniform porosity below the chip region indicated a consistent application of pressure during the sintering process, as shown in Fig. 8 (a) and (b). In Fig. 8 (c), sample A3 exhibited a sintered structure characterized by metallic connections between particles, suggesting a successful sintering procedure. In contrast, sample B1 not only displayed these metallic bonds but also demonstrated epoxy reinforcement. Fig. 8 (d) revealed the infiltration of epoxy into the porous areas through SEM imagery, highlighting its role in enhancing the structural density and bonding integrity of the sintered matrix. Moreover, the electrical conductivity of the sintered material plays a crucial role in determining the effectiveness of the connection. The electrical conductivities of the A3 and B1 joints were examined and found to be $(2.030 \pm 0.169) \times 10^5$ S cm^{-1} and $(1.336 \pm 0.107) \times 10^5$ S cm^{-1}, respectively. These findings indicated that the inclusion of epoxy resin leads to a decrease in the conductive properties.

3.2. High temperature reliability

In order to evaluate the performance of sintered materials in challenging operational conditions within power module service, particularly in intricate temperature environments, high-temperature aging tests and thermal cycling tests were carried out on two optimized sets of sintered joints A3 and B1.

3.2.1. High-temperature storage test

The high-temperature storage test (HST) was conducted at a temperature of 250 °C in order to replicate the operational conditions of power electronics devices in high-temperature environments. After aging for different durations (0 h, 50 h, 100 h, 150 h, 200 h, 300 h, and 400 h), each group of samples, which included ten joint samples on a single DBC substrate, was subjected to shear testing. The results presented in Fig. 9 indicate that the shear strength of the A3 joints initially increased rapidly, reaching 73% (89.44 MPa) of the initial value after 50 h. Subsequently, the shear strength stabilized at around 80 MPa and exhibited slight fluctuations throughout the 100–400 h aging period. On the other hand, the shear strength of the B1 joints exhibited a gradual
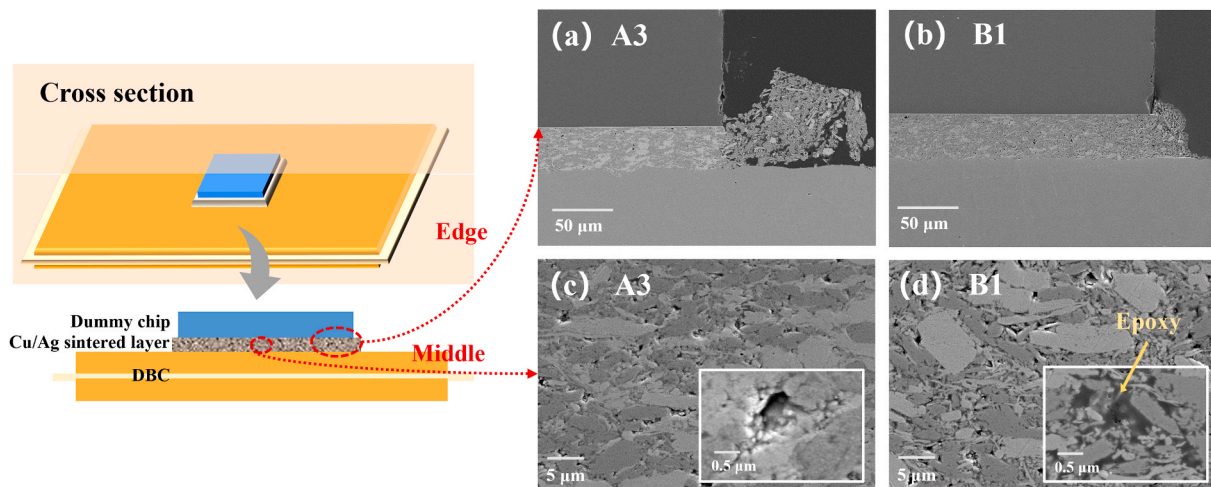

Fig. 8. SEM morphology photos of the (a)edge and (c)middle of the A3 sample, and (b)edge and (d)middle of the B1 sample.
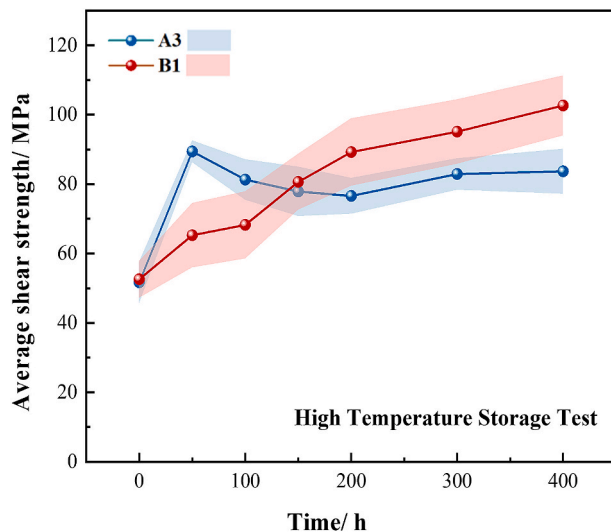
Fig. 9. HST results of the joints fabricated by A3 and B1 pastes. The shaded areas around each line indicate the error bars, representing the standard deviation of the data.

Fig. 10. TCT results of the joints fabricated by A3 and B1 pastes. The shaded areas around each line indicate the error bars, representing the standard deviation of the data.
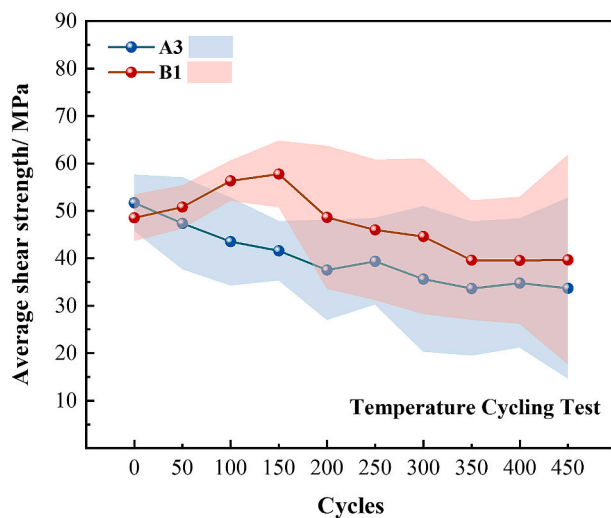
increase, doubling the initial value to 94.75 MPa after 400 h of aging. In addition, *t*-test analysis was also carried out for statical analysis. Tables S1 and S2 presented *t*-test analysis results of shear strength of two groups of samples. It is evident that following a 200-hour aging period, the strength of the B1 joint surpasses that of the A3 joint, thus indicating a noteworthy impact on joint strength improvement during high-temperature aging as a result of the inclusion of epoxy resin.

3.2.2. Temperature cycling test

For power electronics applications, failures are often caused by the mismatch of the coefficients of thermal expansion (CTE) due to the high operating temperatures. Therefore, temperature cycling tests (TCT) are commonly conducted to assess the reliability of die-attach materials. The TCT conditions were set at a range of −55 to 150 °C with 2 cycles per hour. During the experiment, samples consisting of 10 joints each were extracted at regular intervals of 50 cycles to evaluate the shear strength. The corresponding test results were presented in Fig. 10, with the corresponded *t*-test analysis was shown in Tables S3 and S4. For

paste A3, the shear strength of the joints gradually decreased to 35.64 MPa after 300 cycles, and then stabilized around 34 MPa until 450 cycles, demonstrating a consistently high strength. In the case of paste B1, the shear strength initially increased by 19.0%–57.76 MPa after 150 cycles. Subsequently, it decreased and reached a stable level of approximately 40 MPa, which was higher than that of A3 samples but 17.6% lower than the initial strength. We hypothesized that the initial strength increase was attributed to the additional curing of the YD system, which consolidates the findings of HST outlined in Section 3.2.1. It is important to note the increasing size of the error bars for both paste groups after reaching 200 cycles. It is observed that joints B1 showed a higher level of variability. Despite the fact that the lower limits of the B1 error bars persistently surpassed those of A3, implying a potential initial protective effect of the epoxy residues against oxidation. The overall trend, including the mean values, indicated a more pronounced decline in shear strength for B1 after 200 cycles. This suggested that the existence of epoxy residues may potentially contribute to mechanical deterioration over time, thus accelerating failure under the cyclic thermal conditions of the test.

3.3. Evolution of microstructures at high temperatures

To investigate the factors contributing to the alteration in joint strength during high-temperature procedures, cross-sections of joints were prepared with varying durations of high-temperature aging. Subsequently, an in-depth analysis was conducted to examine the changes in microscopic materials and structures over time. Given the occurrence of delamination cracking in both the ceramic layer and the copper clad layer of the DBC substrate during the TCT, the ensuing analysis focused on the test findings of the cross-sectional samples after HST. SEM photos of the cross section of Cu–Ag composite joints produced using A3 and B1 pastes were presented in Fig. 11(a) and (b). These images illustrated the evolution of the joint structure after various aging periods during high-temperature sintering, namely 0 h, 50 h, 100 h, 200 h, and 400 h. It was evident that all the sintered Cu–Ag composite joints exhibited a compact sandwich structure.

The evolution of porosity was determined by extracting and analyzing the sintered layer in Fig. 11 using image J software, as depicted in Fig. 12(b) and Table 2. The analysis results indicate that the porosity of sample A3 decreased from 2.86% in its initial state to 1.89% after 50 h of aging. This decrease is associated with a noticeable increase in shear strength observed in HST. Subsequently, the porosity exhibited a notable increasing trend, reaching 6.72% at 200 h, while the shear strength showed a decline during this stage. From 200 h to 400 h of aging, both the porosity and shear strength remained relatively stable. This analysis demonstrates the close relationship between porosity and changes in shear strength. It is worth noting that the porosity evolution of the B1 group samples, which had epoxy added, displayed a completely different trend. The initial porosity of sample B1 was 1.93%, followed by a fluctuating downward trend in porosity. After 400 h of aging, the cross-sectional sample's porosity was only 0.57%. Correspondingly, the shear strength of the B1 sample gradually increased with aging time, further indicating a negative correlation between porosity and changes in shear strength. Additionally, a more detailed examination of the images following the extraction of porosity revealed a correlation between the distribution of pore sizes and the duration of aging, as illustrated in Fig. 11 (c) and (d). The findings demonstrated a gradual increase in the area occupied by pores in the A3 sample throughout the aging process, which was attributed to the coarsening and growth of the sintering neck [48]. Moreover, an increase in the number of smaller-sized pores was observed after 50 h. Considering the concurrent decrease in porosity, it can be speculated that this change was primarily driven by the oxides generated in the pores. On the other hand, the B1 joint exhibited a different distribution of pore sizes due to the presence of epoxy. The pore areas observed in B1 were smaller than those in A1 and showed a slight increase during the aging process. This phenomenon
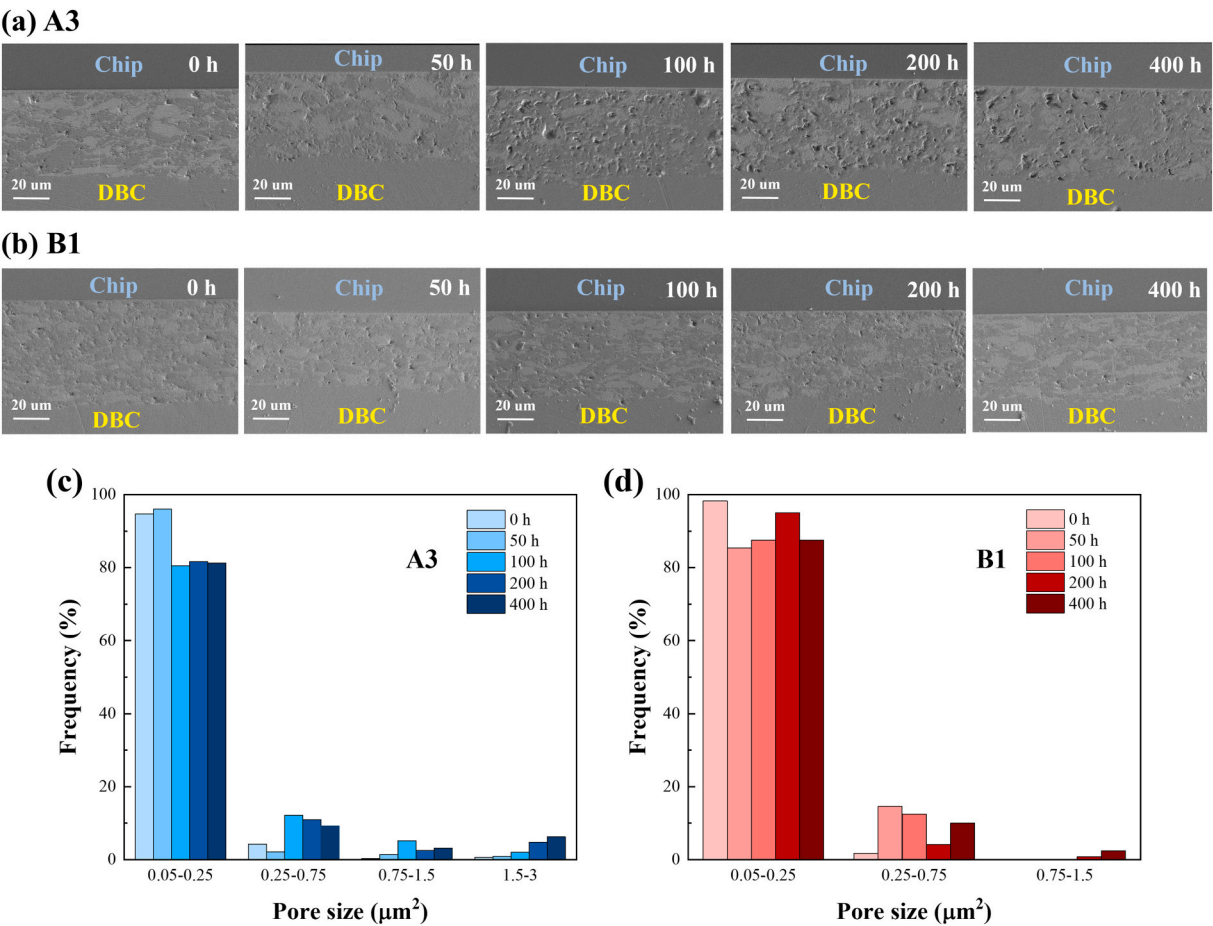
Fig. 11. SEM photos of the cross section of Cu–Ag composite joints fabricated by (a)A3 and (b)B1 pastes after different aging time during HST: 0 h, 50 h, 100 h, 200 h, and 400 h. Pore size distribution for different aging time of (c)A3, (d)B1 sintered samples.
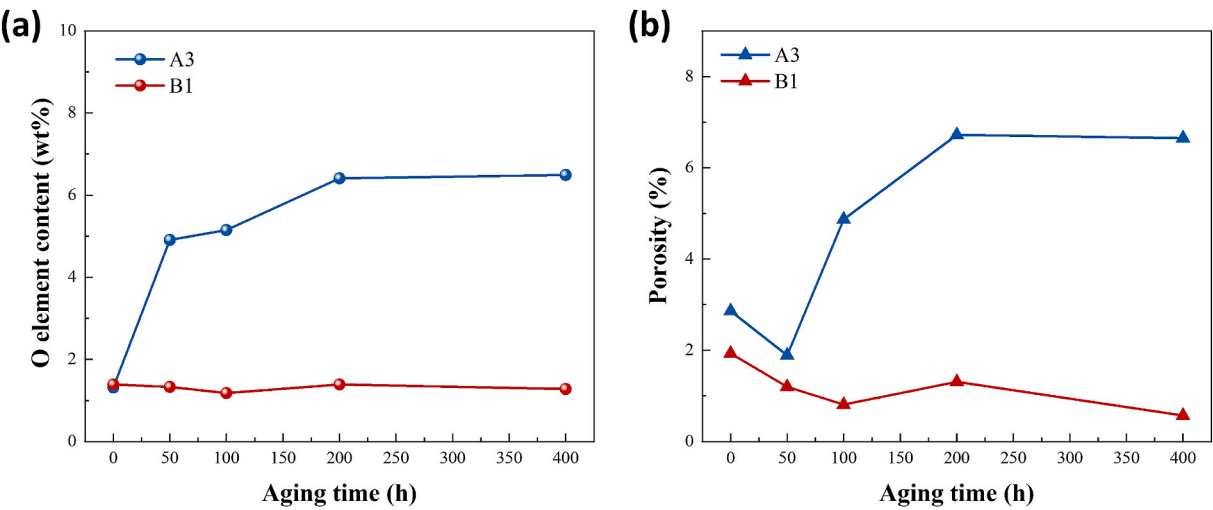

Fig. 12. The change of (a)oxygen element content and (b)porosity of A3 and B1 joints during HST.

Table 2
Porosity from SEM photos.

Sample	0 h	50 h	100 h	200 h	400 h
A3	2.86%	1.89%	4.87%	6.72%	6.65%
B1	1.93%	1.20%	0.81%	1.31%	0.57%

can be attributed to the positive effects of epoxy filling pores, which enhance the structural stability.

Simultaneously, the EDS technique was employed to monitor the variations in the elemental composition of the sintered layer, and the analyzed data were documented in Table 3 and Table 4. The comparison of oxygen content in the two types of joints during the high temperature aging process was presented in Fig. 12(a). The results indicated that the

Table 3
EDS data for A3 joints after HST.

Elements (wt%)	0 h	50 h	100 h	200 h	400 h
Cu	47.14	48.44	47.43	46.36	45.93
Ag	45.88	41.35	41.60	40.79	40.92
C	6.10	5.30	5.82	6.44	6.66
O	1.32	4.91	5.15	6.41	6.49

Table 4
EDS data for B1 joints after HST.

Elements (wt%)	0 h	50 h	100 h	200 h	400 h
Cu	45.85	45.79	46.68	45.41	46.97
Ag	44.58	43.95	43.91	44.19	43.50
C	8.18	8.94	8.23	9.01	8.25
O	1.39	1.33	1.18	1.39	1.28

initial oxygen content of the B1 and A3 samples was 1.32 wt% and 1.39 wt%, respectively, with the B1 sample exhibiting slightly higher oxygen content. Furthermore, the carbon content of the B1 sample (8.18 wt%) was markedly higher compared to the A3 sample (5.30 wt%), suggesting a potential presence of more organic residues in the B1 sample. Over time, as the high-temperature aging period increased, the oxygen content of the B1 sample remained relatively unchanged, stabilizing at approximately 1.3%. In contrast, the oxygen content of the A3 sample experienced a rapid increase to 4.91 wt% after 50 h and continues to gradually increased to 6.49 wt% during subsequent aging processes. This revealed a significant oxidation process taking place in the A3 sample. XPS technology was applied to identify the source of oxides, as

illustrated in Fig. S1. The results indicated that copper was the main contributor to the generation of oxides.

Partial SEM images of the cross-sections at 400 h were recorded in Fig. 13 to facilitate further investigation of the underlying mechanism. By combining the obtained results on porosity and elemental analysis, the deduced aging mechanisms of the two joints were illustrated in Fig. 14. The findings indicated that the further decomposition and volatilization of the PEG residues in A3's joints lead to voids during aging. Consequently, the copper components exposed to elevated temperatures were prone to oxidation, leading to the formation of loosely bound oxides, as depicted in Fig. 13(a). Additionally, the production of oxides allows for the partial filling of pores, thereby enhancing shear strength. However, excessive oxide production contributed to a slight decrease in shear strength. On the other hand, the epoxy resin present in the interstices between the particles of the B1 joints continued to cure, resulting in a more extensive filling of the flaws in the sintered layer, along with the coarsening of the sintering necks between particles. Hence, this phenomenon proves advantageous in terms of improving shear strength. Furthermore, changes in joint structure and elemental composition also affect electrical conductivity. The electrical conductivity tests were conducted on the samples after undergoing 400 h of aging, as detailed in Table S9. After the aging process, the conductivity of samples A3 and B1 decreased by approximately 50.4% and 11.2%, respectively. This demonstrated that, on one hand, epoxy resin had an initial impact on decreasing the electrical conductivity of the specimens. On the other hand, it effectively inhibited the formation of oxides, which enhancing the sintered material's resistance to aging during the HST process.

Combined with the comprehensive analysis of the joints after HST test, we have also speculated on the aging mechanism of the TCT
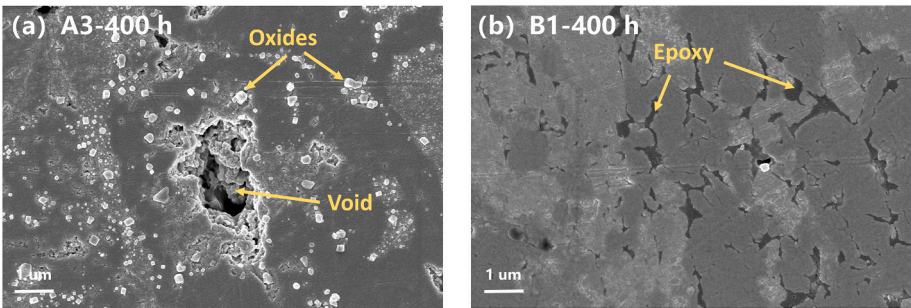

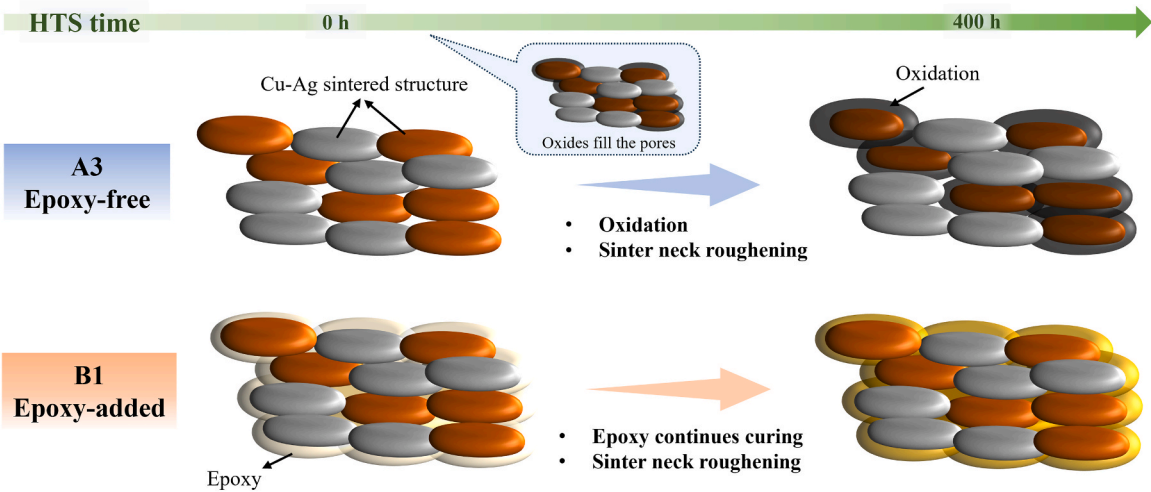**Fig. 13.** Local SEM photos of the joints section after 400 h HST, fabricated by (c)A3 and (d)B1 paste.

Fig. 14. Schematic diagram of the aging mechanism of sintered structures during HST test.
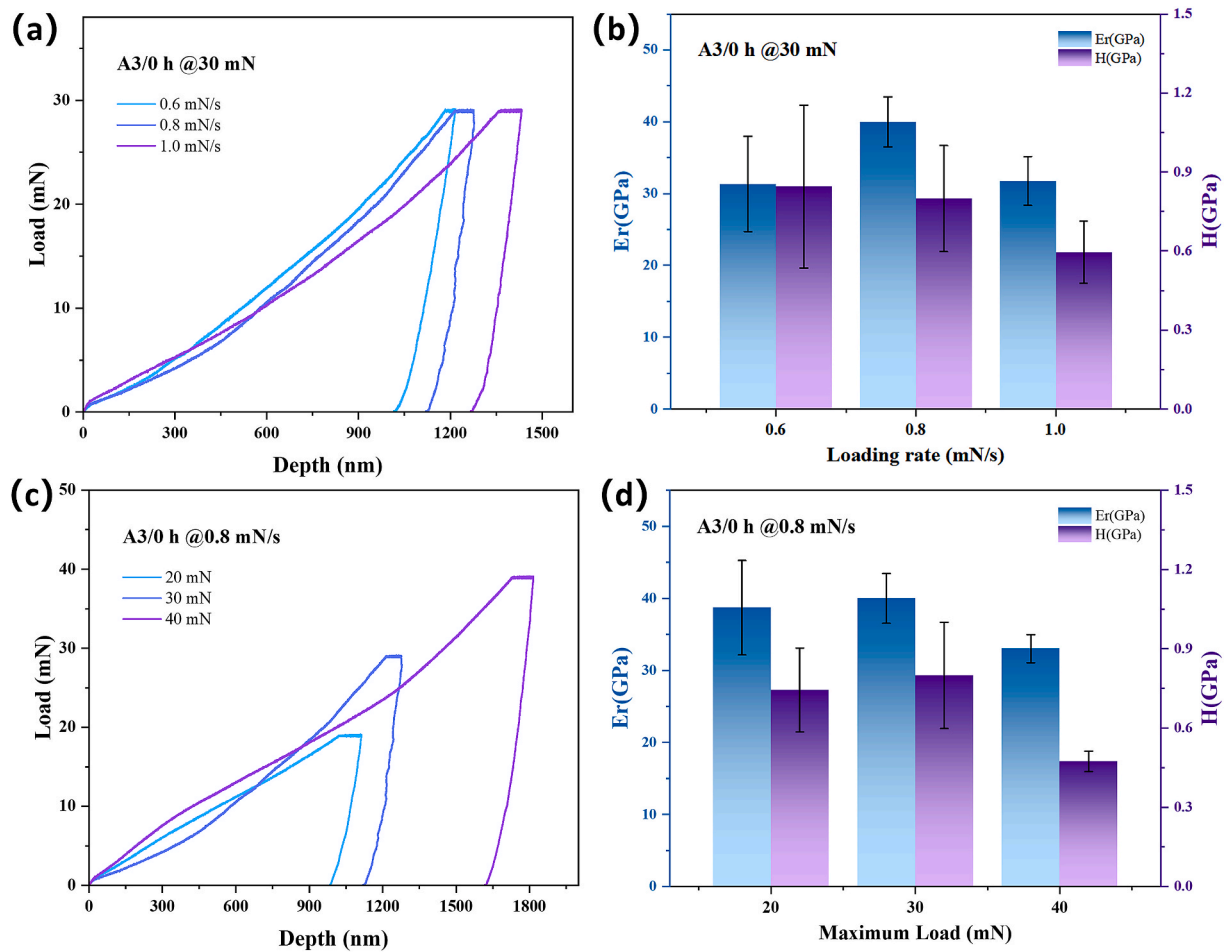
Fig. 15. Effect of loading rate on the indentation properties of A3 joints: (a) Load-depth curve, (b) modulus and hardness; Effect of applied load on the indentation properties of A3 joints: (c) Load-depth curve, (d) modulus and hardness.

samples. Compared to HST aging, TCT aging poses an additional risk of failure due to the mismatch of thermal expansion coefficients (CTE) during high and low temperature cycles. In the case of the A3 samples, the continuous formation of oxides at high temperatures exacerbated the CTE mismatch issue during temperature cycles, leading to a gradual decrease in shear strength. As for the B1 group samples, the enhanced curing of the epoxy component during the high temperature stage of TCT might be the main factor behind the initial increase in shear strength within the first 150 cycles. However, as the temperature shock caused a progressive increase in cracks resulting from the CTE mismatch among the different components, the shear strength subsequently declined.

3.4. Evolution of micromechanical properties at high temperatures

Changes in microstructure during high-temperature evolution also had impacts on micromechanical properties. The utilization of nano-indentation technology enabled accurate and efficient detection, thereby facilitating a comprehensive understanding of joint performance at various aging periods. Additionally, this technology assists in predicting the long-term reliability of joints. To maintain the experiment's consistency, the areas selected for the nanoindentation experiment were all performed close to the central position of the sintered layer.

3.4.1. Main influencing factors of room temperature nanoindentation test

A judicious choice of parameters contributes to acquiring dependable data, fostering a comprehensive comprehension of the mechanical

characteristics exhibited by materials at the nanoscale, and furnishing crucial insights for material design and performance enhancement. The crux of the matter about selecting suitable parameters for nano-indentation tests lies in ensuring that the tests faithfully capture the mechanical properties inherent to the material. As depicted in Figs. 15 and 16, the figures illustrated the influence of various loading speeds and load test conditions on the Load-depth curves and the calculated micromechanical performance parameters of the unaged A3 and B1 samples in their initial state. During the test, the samples initially underwent elastic-plastic deformation during the loading process of the indenter, with the elastic deformation recovering during the unloading process. When subjected to the same load, the A3-0 h sample exhibited deeper indentation with an increasing loading rate. However, there was no positive correlation between the loading rate and the indentation depth for the B1-0 h sample. Under the same load, both samples demonstrated that higher loading rates resulted in deeper indentation depths. We hypothesized that this difference was due to variations in the elastic deformation absorption of the epoxy filler during the loading stage of the B1-0 h sample, suggesting that the addition of epoxy may have potential advantages in improving the load impact resistance of the joint. Furthermore, the obtained data on hardness and elastic modulus under different test conditions were compared. The results indicated that the hardness and modulus values of the A3-0 h sample were more sensitive to changes in test parameters compared to those of the B1-0 h sample. Excessive load and loading rate led to a decrease in the calculated hardness and elastic modulus values of the A3-0 h sample, and also resulted in a more pronounced indentation size effect. Finally, after a comprehensive comparison, the loading speed of 0.8 mN/s and the
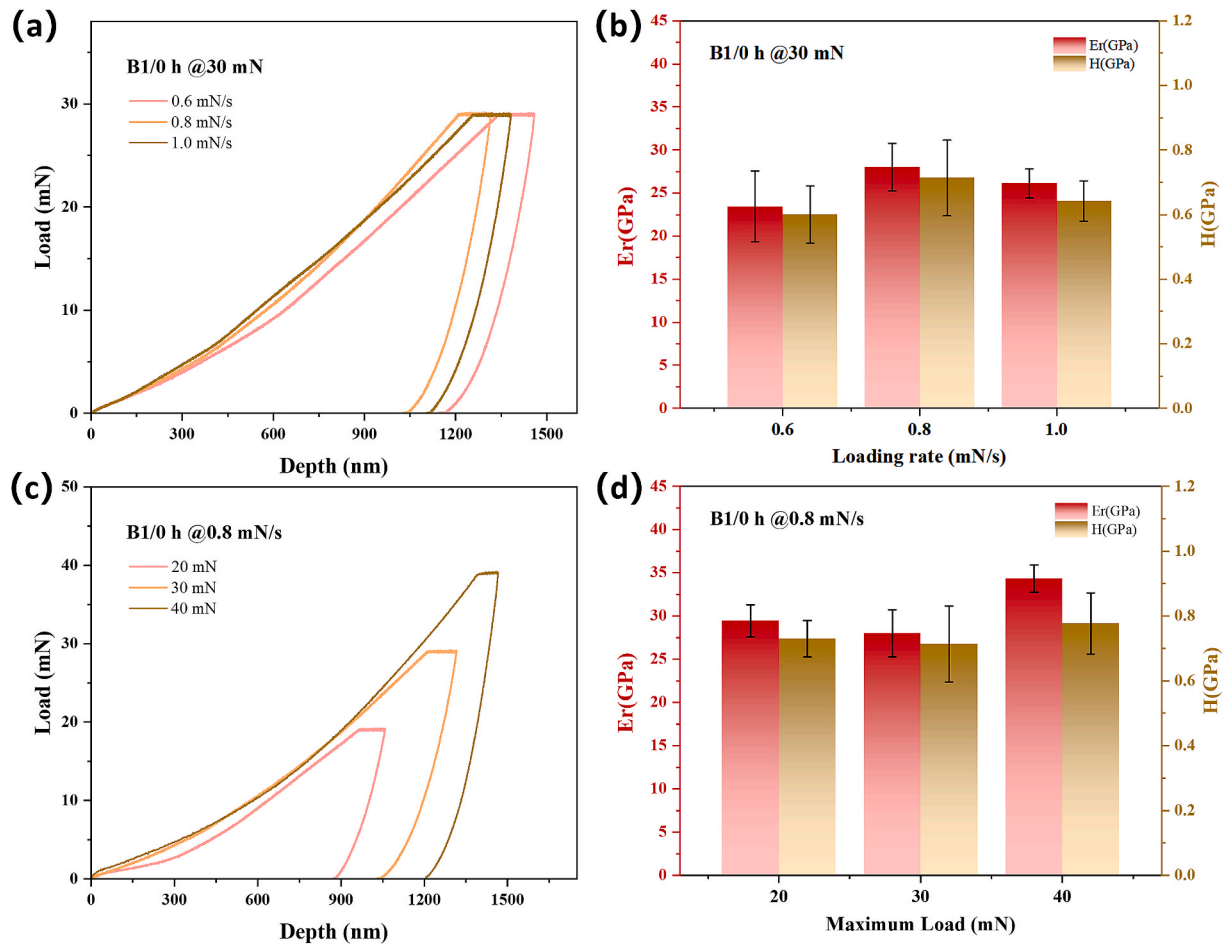
Fig. 16. Effect of loading rate on the indentation properties of B1 joints: (a) Load-depth curve, (b) modulus and hardness; Effect of applied load on the indentation properties of B1 joints: (c) Load-depth curve, (d) modulus and hardness.
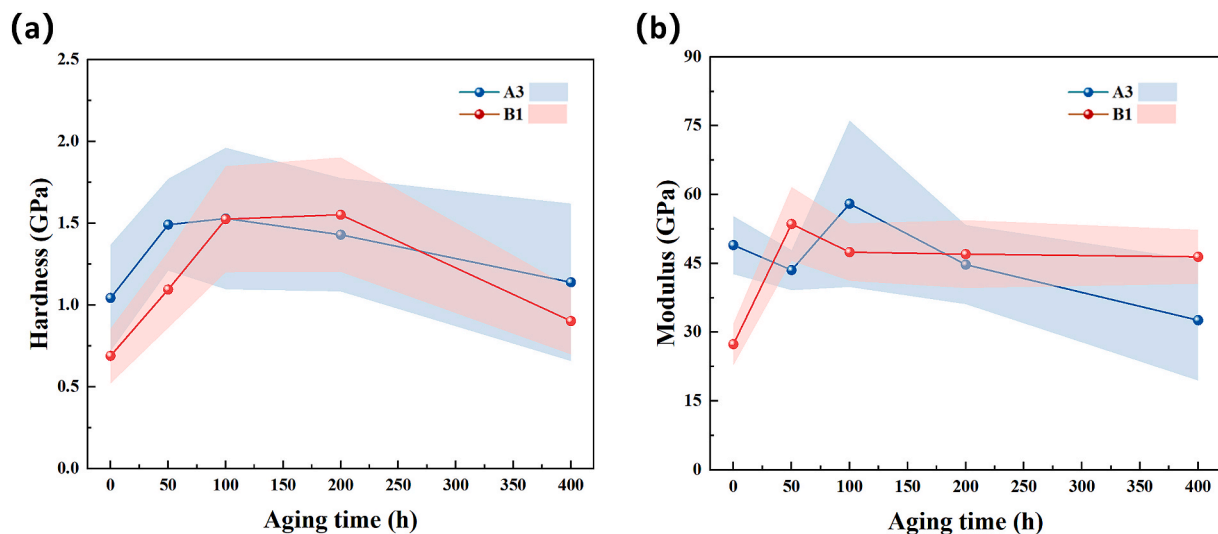

Fig. 17. (a) Hardness and (b) modulus of Cu–Ag composite sintered samples after different HST aging time. The shaded areas around each line indicate the error bars, representing the standard deviation of the data.

applied load of 30 mN were chosen as the set parameters for subsequent experiments.

3.4.2. Hardness and elasticity modulus

With the advantages of high resolution and non-destructive testing provided by nanoindentation technology, it becomes possible to measure the hardness and elastic modulus of materials on a microscopic scale. This capability proves instrumental in monitoring and evaluating the evolution of microscopic properties of materials during the aging process.
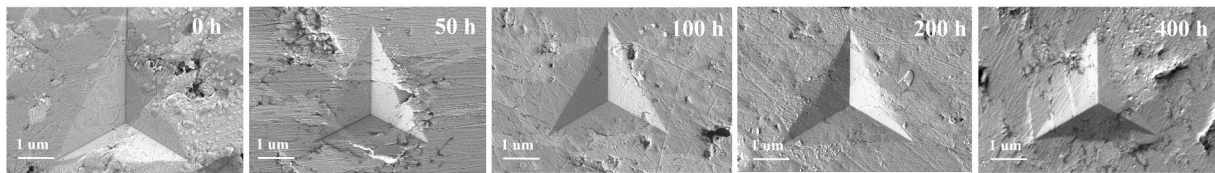
(a) A3
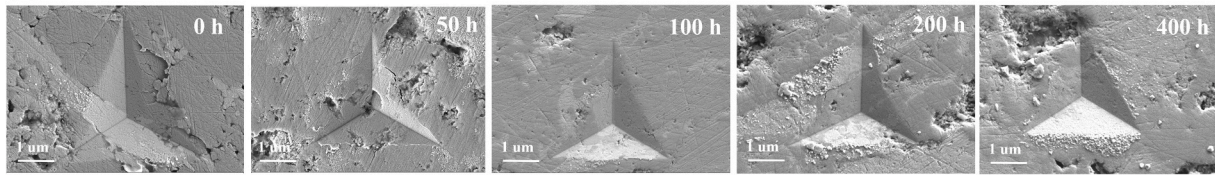
(b) B1

Fig. 18. The indentation morphologies of (a) A3 and (b) B1 cross-section samples at different high temperature aging time.

Fig. 17 exhibited the evolution process of the average hardness and elastic modulus of Cu–Ag composite joints as a function of the aging time of HST. Table S5 ~S8 recorded the relevant *t*-test analysis of the two groups of samples during the aging process. Firstly, in terms of hardness, both the A3 and B1 joints exhibited a pattern of initially increasing and then decreasing during the aging process. For the A3 sample, the initial hardness was 1.04 GPa. After 100 h of aging, the hardness reached its peak at 1.53 GPa, and subsequently decreased to 1.14 GPa after 400 h, representing a 9.6% increase compared to the initial hardness. In contrast to A3, the initial hardness of B1 was lower at 0.69 GPa. After 200 h of aging, it achieved the highest average hardness of 1.55 GPa, which was 2.24 times the initial hardness, and then declined to 0.90 GPa, which was 30.4% higher than the initial hardness. Furthermore, there was a slight discrepancy in the evolution of the modulus. The A3 sample exhibited a fluctuating downward trend, with an initial modulus of 48.98 GPa decreasing by 33.4% to 32.61 GPa after 400 h of high-temperature aging. However, in the case of the B1 sample, the modulus demonstrated an upward trend. The initial modulus was 27.37 GPa, and after aging, it steadily increased to approximately 47 GPa. Generally, the initial hardness and elastic modulus of the joint were diminished upon the addition of epoxy. Nevertheless, as high-temperature aging progresses, the interstitial effect and subsequent solidification of the epoxy, coupled with continued diffusion between copper and silver particles, contributed to the heightened resistance to plastic deformation demonstrated by the B1 joint.

3.4.3. Creep behavior

Moreover, nanoindentation technology is also a useful tool for quantifying the creep properties of materials at the nanoscale. Through the investigation of creep behavior, we can acquire noticeable insights into the deformation mechanisms of materials subjected to prolonged stress, thereby enhancing our comprehension of material stability and reliability. To examine the progression of creep characteristics during high temperature aging, an investigation was conducted on two kinds of Cu–Ag blend joints with different aging times. These samples were loaded at a force of 30 mN for a duration of 300 s. Each sample was tested 10 times, and the maximum creep depth showed a normal distribution, as shown in Fig. 20(a). The curve with the maximum creep depth closest to the average value was selected as a representative for subsequent analysis. The obtained indentation morphologies were presented in Fig. 18, while the corresponding creep curves were shown in Fig. 19. In the initial state at 0 h, the creep displacement depth of sample A3 exceeded that of B1, measuring 102.8 nm and 78.9 nm, respectively. Following high-temperature aging, the creep depth of the A3 sample exhibited a pattern of initially decreasing to 35.6 nm, then increasing, and eventually stabilizing at approximately 50 nm during the aging process spanning from 200 to 400 h. This value accounted for 50% of the initial creep depth. For the B1 samples, the creep depth gradually reduced and stabilized at roughly 37 nm after aging for 100 h, which was much lower than the creep depth of the A3 sample after long-term aging, showing better creep resistance.

The strain rate sensitivity index (*m*) of Cu–Ag composited joints was calculated to provide a more in-depth investigation into the creep
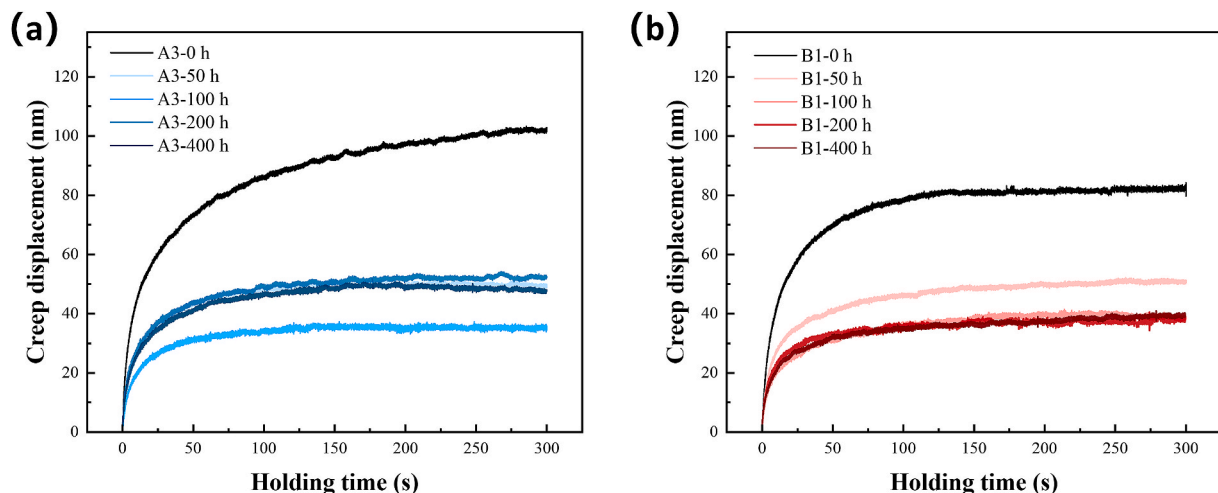

Fig. 19. Creep behavior of (a) A3 and (b) B1 samples after different HST aging time.
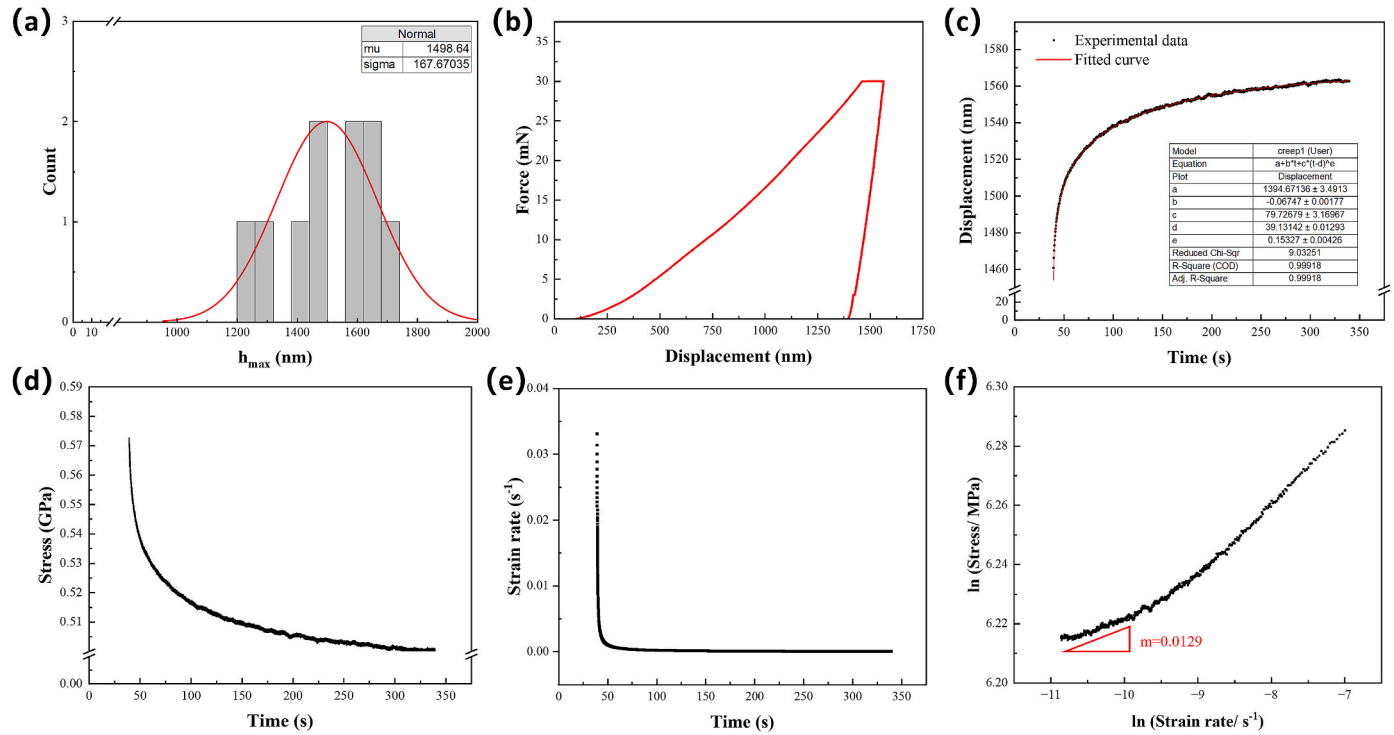
Fig. 20. (a) Maximum indentation depth on A1-0 h sample; (b) Force-displacement curve of A1-0 h sample. The holding time was 300 s during the creep stage under 20 mN. (c) Displacement-time, (d) stress-time, (e) strain rate-time, (f) natural logarithmic stress versus natural logarithmic creep stain rate curves during the creep stage at (b).

Table 5
Fitting parameters of Cu–Ag composited samples with different aging times.

Sample	a	b	c	d	e	Agj.R-Square	m
A3-0 h	1394.671	−0.067	79.727	39.131	0.153	0.99918	$1.29*10^{-2}$
A3-50 h	795.915	−0.071	292.277	36.754	0.038	0.99524	$6.67*10^{-4}$
A3-100 h	799.100	−0.045	203.363	37.277	0.035	0.98887	$2.91*10^{-4}$
A3-200 h	942.161	−0.061	78.518	37.569	0.103	0.99587	$2.30*10^{-3}$
A3-400 h	1044.51	−0.086	40.465	37.785	0.171	0.99594	$1.39*10^{-3}$
B1-0 h	793.087	−0.118	430.496	37.021	0.043	0.99923	$2.80*10^{-3}$
B1-50 h	849.331	−0.034	323.006	37.383	0.028	0.99665	$2.52*10^{-3}$
B1-100 h	1028.896	−0.059	21.431	37.708	0.212	0.99277	$2.22*10^{-3}$
B1-200 h	945.630	−0.082	72.608	37.699	0.135	0.99064	$2.43*10^{-3}$
B1-400 h	1077.818	−0.020	281.540	37.594	0.023	0.98952	$2.49*10^{-3}$

mechanism of the two joints across varying aging durations. The calculation process of A1-0 h joint was shown as an example in Fig. 20 (b)~(f): Firstly, the empirical formula was utilized to fit and creep displacement-time curves.

$$h = a + bt + c(t - d)^e \tag{14}$$

where h is the creep displacement, t is the creep time and parameters a, b, c, d, and e are constants [36]. Fitting parameters of Cu–Ag composited samples with different aging times were listed in Table 5. Next, the values of $\dot{\varepsilon}$ and σ calculated by Eqs. (7) and (8) were plotted with respect to creep time in Fig. 20(d) and (e). Subsequently, the double logarithmic curves of $\dot{\varepsilon}$ and σ were presented in Fig. 20(f). Finally, the value of m was determined based on the steady-state stage of creep, specifically using the fitting region indicated by the red triangle.

Afterwards, strain rate sensitivity index m of the A3 and B1 samples after different high temperature aging time were presented in Fig. 21. According to previous research on nanoindentation, there exist three plausible mechanisms for creep, namely grain boundary sliding, diffusional creep, and dislocation power-law creep [36,39,49–51]. When the value of m is equal to 1, the primary governing factor for creep is the

diffusion of atoms through lattice diffusion or Coble creep [39]. When m equals 0.5, creep behavior is primarily controlled by grain boundary sliding [49]. And, when m is less than 0.33, the predominant mechanism for creep is dislocation power-law creep [50,51]. Hence, the results presented herein were all found to be below 0.33, indicating that dislocation creep served as the prevailing mechanism in all of the aforementioned samples. Furthermore, in the case of the A3 samples, the value of m initially exhibited a substantial decrease from 0.0129 to 0.000291 at 100 h, subsequently increasing to 0.00139 at 400 h. This observation suggested that the introduction of oxides generated at elevated temperatures effectively impeded the movement of dislocations. However, an excessive amount of loosely oxides in Cu–Ag joint proved detrimental to the material's ability to resist creep. As for the B1 sample, the value of m fluctuated between 0.002 and 0.0025, thereby indicating that benefit to epoxy addition, the internal structure of the joint experienced minimal alteration due to high-temperature aging. The modest fluctuations in the values might be attributed to surface irregularities such as holes and roughness. Overall, the low strain rate sensitivity index values obtained for both samples point to the commendable creep resistance of the Cu–Ag joints.
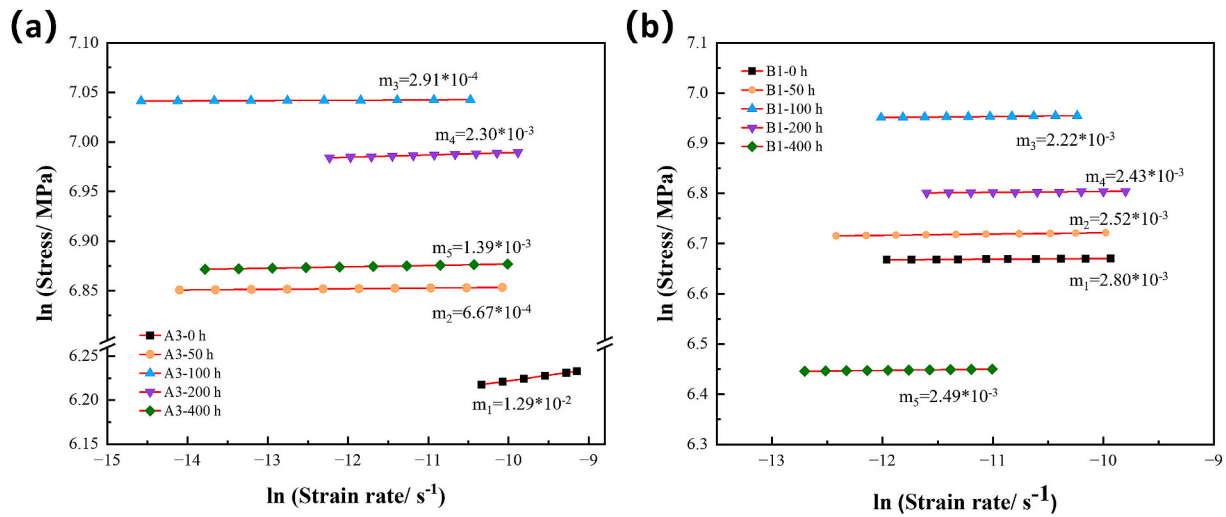
Fig. 21. Natural logarithmic stress versus natural logarithmic creep stain curves of Cu–Ag samples after different high temperature aging time: (a) A3, (b) B1.Fig. 20 Natural logarithmic stress versus natural logarithmic creep stain curves of Cu–Ag samples after different high temperature aging time: (a) A3, (b) B1.

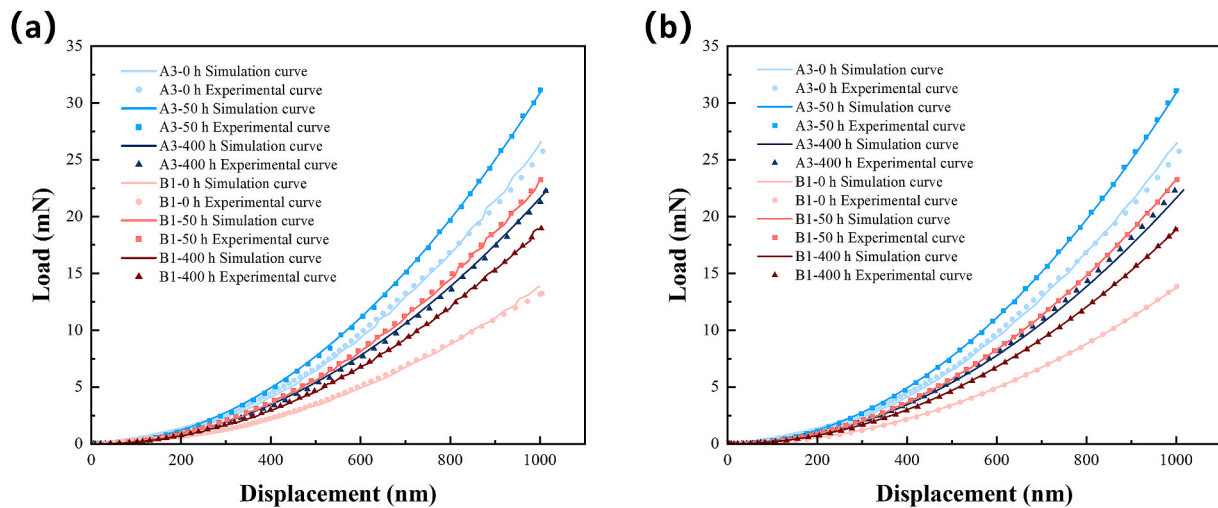

Fig. 22. Comparison of load-displacement curves predicted by the elastoplastic model of Cu–Ag composite sintered joints with experimental results: (a) n = 0, (b) n≠0.

3.4.4. Constitutive behavior

Establishing a constitutive model can help simulate the elastic-plastic response of materials under different conditions and provide reliability assessment for the overall structural design of the power module [27]. In this study, we employed an inversion analysis method grounded in the FEM to investigate the variances in the constitutive relationships of sintered joints from two solvent systems at distinct high-temperature aging stages. Given the sudden alterations observed in the shear strength, porosity, and oxygen content of the samples after undergoing a 50-h aging process, we have opted to examine and compare samples that were aged at high temperatures for 0 h, 50 h, and 400 h to conduct a more comprehensive analysis.

The inverse analysis algorithm was primarily based on the nano-indentation loading stage curve. Initially, an ideal elastic-plastic model was assumed with a stress enhancement index of 0 (n = 0). The load-displacement curves were obtained by using the FEM and performing iterative computations until the relative error of the nanoindentation results were less than 0.5%, as shown in Fig. 22(a). Then, the stress enhancement index n, obtained through dimensional theoretical analysis, was replaced by simulation for further iterative optimization, as shown in Fig. 22(b). The validity and accuracy of the constitutive

relationships determined through inversion analysis were confirmed by comparing the FEM results with experimental data. The Von Mises stress cloud diagrams of each selected Cu–Ag composited sintered sample under nanoindentation simulation were presented in Fig. 23. Table 6 provided the constitutive parameters of the samples. The stress-strain relationships of the selected samples were expressed by formulas (15) to (20) respectively, and the corresponding stress-strain curves were plotted in Fig. 24. The results indicated that the A3 samples, without epoxy before HST aging, possessed a yield stress (σ_y) of 107.26 MPa, which was 8.45 times greater than the initial σ_y of 12.70 MPa observed in the B1 sample with epoxy added. It is noteworthy, however, that evident differences were observed in joints with different solvent systems following aging. After 50 h of aging, the σ_y of the A3 sample substantially increased to 197.63 MPa, but then decreased to 40.55 MPa after 400 h of exposure to high temperatures. The considerable fluctuations in the σ_y of the A3 sample indicated the instability of the exposed Cu–Ag composited joints in a prolonged high-temperature environment. Over time, the formed oxides would eventually compromise the integrity of the joint, leading to a decline in mechanical properties. Conversely, the performance of the B1 sample remained relatively stable. The σ_y increased to 54.66 MPa after 50 h of high-temperature aging,

(a) A3-0 h

(b) A3-50 h

(C) A3-400 h

(d) B1-0 h

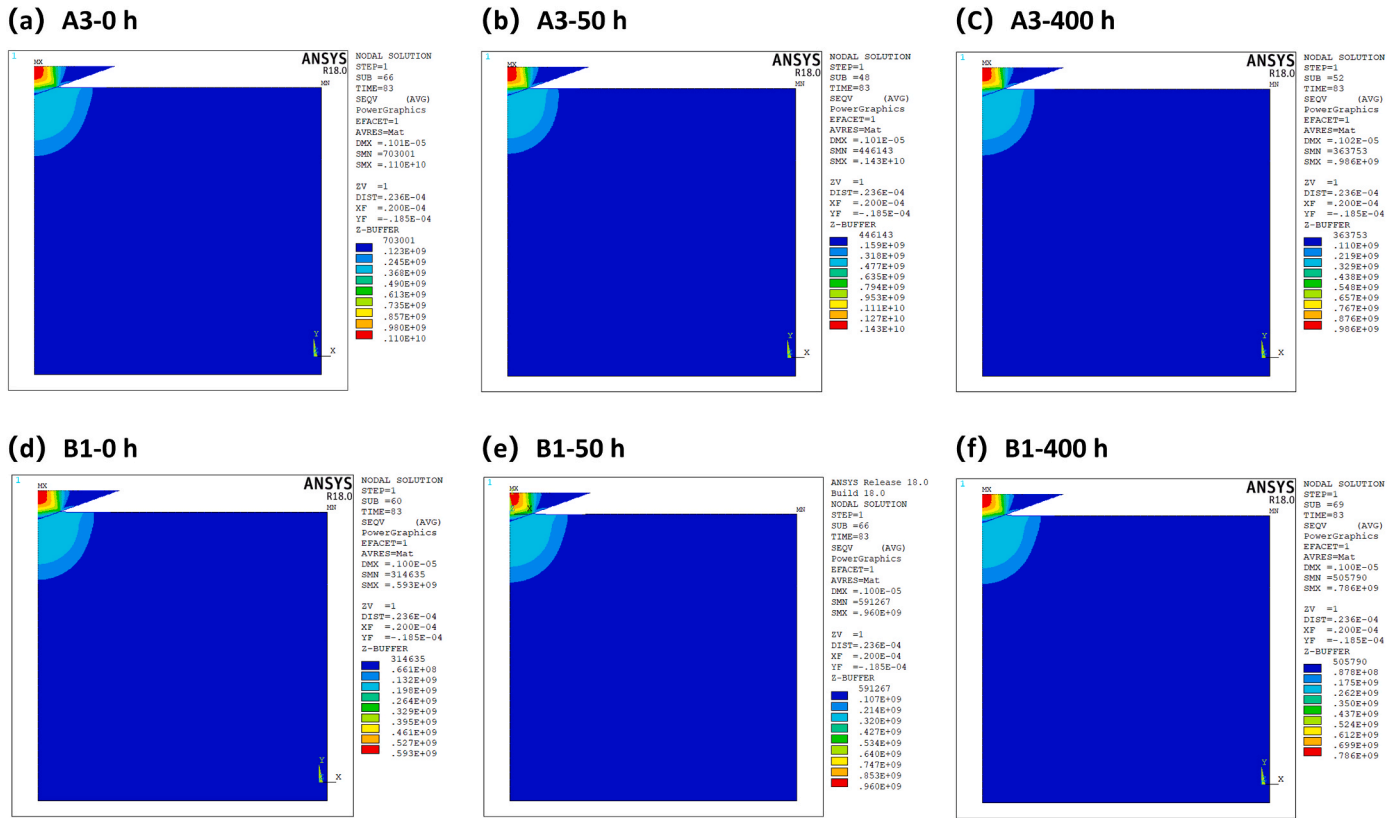**(e) B1-50 h**

(f) B1-400 h

Fig. 23. Results of Von Mises stress contours in finite element simulation: (a) A3-0 h, (b) A3-50 h, (c) A3-400 h; (d) B1-0 h, (e) B1-50 h, (f) B1-400 h.

Table 6
Constitutive parameters of Cu–Ag composited sintered samples.

Sample	W_p/W_t	h_r/h_m	σ_r (MPa)	n	ε_r	σ_y (MPa)
A3-0 h	0.86796	0.90268	323.20	0.4104	0.02579	107.26
A3-50 h	0.77488	0.83596	455.91	0.4210	0.02913	197.63
A3-400 h	0.86796	0.90268	306.67	0.6684	0.02550	40.55
B1-0 h	0.81780	0.86676	177.78	0.6616	0.02601	12.70
B1-50 h	0.85765	0.89529	282.08	0.5198	0.02510	54.66
B1-400 h	0.86834	0.90295	230.65	0.4769	0.02604	53.42

which was 4.30 times the initial value. However, the σ_y remained consistent at 53.42 MPa after a longer aging period of 400 h. The noticeable disparity between the two joints demonstrated that the addition of epoxy reduced the joint's resistance to plastic deformation. Nevertheless, further curing of the epoxy after a specific aging time effectively enhanced its ability to withstand plastic deformation. To sum up, the protective effect of epoxy on the internal microstructure can enhance the mechanical stability of the joint during high-temperature aging.

A3-0 h:

$$\sigma = \begin{cases} 56950\varepsilon & (\sigma \leq 107.26) \\ 107.26\left(1 + 530.95\varepsilon_p\right)^{0.4104} & (\sigma > 107.26) \end{cases} \tag{15}$$

A3-50 h:

$$\sigma = \begin{cases} 42620\varepsilon & (\sigma \leq 197.63) \\ 197.63\left(1 + 215.66\varepsilon_p\right)^{0.4210} & (\sigma > 197.63) \end{cases} \tag{16}$$

A3-400 h:

$$\sigma = \begin{cases} 31230\varepsilon & (\sigma \leq 40.55) \\ 40.55\left(1 + 770.16\varepsilon_p\right)^{0.6684} & (\sigma > 40.55) \end{cases} \tag{17}$$

B1-0 h:

$$\sigma = \begin{cases} 27420\varepsilon & (\sigma \leq 12.7) \\ 12.7\left(1 + 2161.42\varepsilon_p\right)^{0.6616} & (\sigma > 12.7) \end{cases} \tag{18}$$

B1-50 h:

$$\sigma = \begin{cases} 49000\varepsilon & (\sigma \leq 54.66) \\ 54.66\left(1 + 896.45\varepsilon_p\right)^{0.5198} & (\sigma > 54.66) \end{cases} \tag{19}$$

B1-400 h:

$$\sigma = \begin{cases} 42020\varepsilon & (\sigma \leq 53.42) \\ 53.42\left(1 + 786.60\varepsilon_p\right)^{0.4769} & (\sigma > 53.42) \end{cases} \tag{20}$$

4. Conclusions

In this study, four types of alcohol-based pastes (A1~4) and four types of epoxy-based pastes (B1~4) containing micron-scale Cu–Ag composite particles were developed and manufactured to substitute sintered pure silver or copper joints for die-attach. The viscosity, shear strength, high-temperature reliability, and micromechanical properties of the optimized samples were analyzed. The primary findings are outlined below.

(1) The influence of the solvent system on sintered joints is of utmost importance. The viscosity of the solvents with the epoxy addition was found to be higher. Additionally, the results of DCS-TGA analysis revealed that the organic residual content in the joints was also higher. The maximum shear strength achieved in each group was 51.70 MPa (A3) and 48.54 MPa (B1), respectively.

(2) The B1 joints exhibited significantly superior shear strength performance compared to A3 in the conducted reliability tests. Following 400 h of high-temperature aging, the average shear strengths of A3 and B1 were measured at 79.92 MPa and 94.57 MPa, respectively. Furthermore, even after undergoing thermal
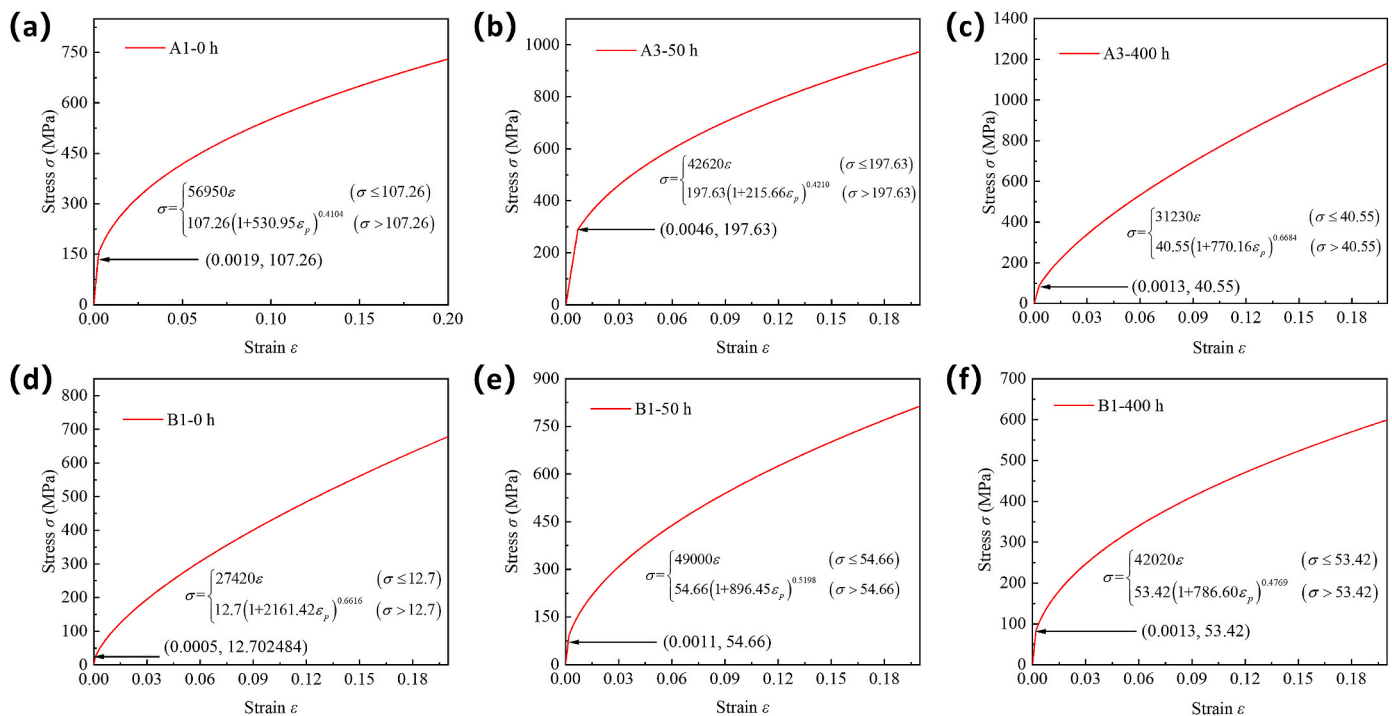
Fig. 24. Elastoplastic constitutive model of Cu–Ag composite joints: (a) A3-0 h, (b) A3-50 h, (c) A3-400 h; (d) B1-0 h, (e) B1-50 h, (f) B1-400 h.

cycling aging, the average shear strengths remained at approximately 34 MPa and 40 MPa for A3 and B1, respectively.

(3) Further microstructure analysis using SEM/EDS and XPS revealed that the isolation oxidation, pore filling, and subsequent solidification of epoxy resin were the primary factors contributing to variations in the aging mechanism of joints fabricated by different solvent systems. These variations ultimately lead to differences in joint performance.

(4) The micromechanical properties of Cu–Ag joints following the aging process were assessed using nanoindentation technology, encompassing the evaluation of hardness, elastic modulus, and creep properties. The findings indicated that the mechanical properties of the B1 sample exhibited comparatively minor alterations after being subjected to high-temperature aging. Moreover, the establishment of elastic-plastic constitutive models for the two Cu–Ag sintered materials offered valuable insight for a comprehensive examination of their mechanical properties and longevity.

In conclusion, the design proposed in this article, which involved incorporating an epoxy component into the solvent of micron particle Cu–Ag, not only yielded a substantially high mechanical strength but also demonstrated reliable performance at high temperatures. This design offered a cost-effective solution for power electronics packaging. Further research could be concentrated on exploring various types and quantities of epoxy components to enhance the reliability of micron-scale copper-silver composite joints in future applications.

Declaration of competing interest

The authors declare that they have no known competing financial interests or personal relationships that could have appeared to influence the work reported in this paper.

Acknowledgments

Appendix A. Supplementary data

Supplementary data to this article can be found online at https://doi.org/10.1016/j.jmrt.2024.05.196.

References

[1] Moreno G, Narumanchi S, Feng X, Anschel P, Myers S, Keller P. Electric-drive vehicle power electronics thermal management: current status, challenges, and future directions. J Electron Packag 2022;144(1). https://doi.org/10.1115/1.4049815.

[2] Qin Y, Albano B, Spencer J, Lundh JS, Wang B, Buttay C, Tadjer M, DiMarino C, Zhang Y. Thermal management and packaging of wide and ultra-wide bandgap power devices: a review and perspective. J Phys Appl Phys 2023;56(9). https://doi.org/10.1088/1361-6463/acb4ff.

[3] Wang Y, Ding Y, Yin Y. Reliability of wide band gap power electronic semiconductor and packaging: a review. Energies 2022;15(18). https://doi.org/10.3390/en15186670.

[4] Paknejad SA, Mannan SH. Review of silver nanoparticle based die attach materials for high power/temperature applications. Microelectron Reliab 2017;70:1–11. https://doi.org/10.1016/j.microrel.2017.01.010.

[5] Manikam VR, Kuan Yew C. Die attach materials for high temperature applications: a review. IEEE Trans Compon Packag Manuf Technol 2011;1(4):457–78. https://doi.org/10.1109/tcpmt.2010.2100432.

[6] Zhang H, Minter J, Lee N-C. A brief review on high-temperature, Pb-free die-attach materials. J Electron Mater 2018;48(1):201–10. https://doi.org/10.1007/s11664-018-6707-6.

[7] Nishimoto M, Tokura R, Nguyen MT, Yonezawa T. Copper materials for low temperature sintering. Mater Trans 2022;63(5):663–75. https://doi.org/10.2320/matertrans.MT-N2021004.

[8] Chen TF, Siow KS. Comparing the mechanical and thermal-electrical properties of sintered copper (Cu) and sintered silver (Ag) joints. J Alloys Compd 2021;866. https://doi.org/10.1016/j.jallcom.2021.158783.

[9] Yang H. Study on the preparation process and sintering performance of doped nano-silver paste. Rev Adv Mater Sci 2022;61(1):969–76. https://doi.org/10.1515/rams-2022-0273.

[10] Peng P, Hu A, Gerlich AP, Zou G, Liu L, Zhou YN. Joining of silver nanomaterials at low temperatures: processes, properties, and applications. ACS Appl Mater Interfaces 2015;7(23):12597–618. https://doi.org/10.1021/acsami.5b02134.

[11] Liu J, Mou Y, Peng Y, Sun Q, Chen M. Novel Cu-Ag composite nanoparticle paste for low temperature bonding. Mater Lett 2019;248:78–81. https://doi.org/10.1016/j.matlet.2019.03.133.

[12] Hsiao C-H, Kung W-T, Song J-M, Chang J-Y, Chang T-C. Development of Cu-Ag pastes for high temperature sustainable bonding. Mater Sci Eng, A 2017;684:500–9. https://doi.org/10.1016/j.msea.2016.12.084.

[13] Chen C, Kim D, Liu Y, Sekiguchi T, Su Y, Long X, Liu C, Liu C, Suganuma K. Development of micron-sized Cu–Ag composite paste for oxidation-free bare Cu bonding in air condition and its deterioration mechanism during aging and power cycling tests. J Mater Res Technol 2023;24:8967–83. https://doi.org/10.1016/j.jmrt.2023.05.104.

[14] Li K, Liu Y, Zhang J, Xiao N. A low cost multi-shapes designed sintering composite paste: A strengthening method of sintered interconnect for die attach in high temperature applications. Mater Lett 2022;315. https://doi.org/10.1016/j.matlet.2022.131884.

[15] Li XYJ, Shi T, Cheng C, Fan J, Cheng S, Li T, Liao G, Tang Z. Depressing of Cu-Cu bonding temperature by compositing Cu nanoparticle paste with Ag nanoparticles. J Alloys Compd: An Interdisciplinary Journal of Materials Science and Solid-state Chemistry and Physics 2017;709:700–7. https://doi.org/10.1016/j.jallcom.2017.03.220.

[16] Tan KS, Cheong KY. Mechanical properties of sintered Ag–Cu die-attach nanopaste for application on SiC device. Mater Des 2014;64:166–76. https://doi.org/10.1016/j.matdes.2014.07.033.

[17] Won M, Kim D, Yang H, Oh C. Low-temperature sinterable Cu@Ag paste with superior strength driven by pre-heating process. Energies 2023;16(14). https://doi.org/10.3390/en16145419.

[18] Choi EB, Lee Y-J, Lee J-H. Rapid sintering by thermo-compression in air using a paste containing bimodal-sized silver-coated copper particles and effects of particle size and surface finish type. J Alloys Compd 2022;897. https://doi.org/10.1016/j.jallcom.2021.163223.

[19] Gao Q, Zhou W, Xia Z, Wang X, Wang Y, Yue Z, Guo F. Investigation of ethylene glycol, α-terpineol, and polyethylene glycol 400 on the sintering properties of Cu–Ag core–shell micro/nano-mixed paste. J Mater Sci Mater Electron 2023;34 (21). https://doi.org/10.1007/s10854-023-10965-y.

[20] Lee CH, Choi EB, Lee J-H. Characterization of novel high-speed die attachment method at 225 °C using submicrometer Ag-coated Cu particles. Scripta Mater 2018;150:7–12. https://doi.org/10.1016/j.scriptamat.2018.02.029.

[21] Kim MI, Lee J-H. Die sinter bonding in air using Cu@Ag particulate preform and rapid formation of near-full density bondline. J Mater Res Technol 2021;14:1724–38. https://doi.org/10.1016/j.jmrt.2021.07.059.

[22] El-Kady MM, Ansari I, Arora C, Rai N, Soni S, Verma DK, Singh P, Mahmoud AED. Nanomaterials: a comprehensive review of applications, toxicity, impact, and fate to environment. J Mol Liq 2023;370. https://doi.org/10.1016/j.molliq.2022.121046.

[23] Khazaka R, Mendizabal L, Henry D. Review on joint shear strength of nano-silver paste and its long-term high temperature reliability. J Electron Mater 2014;43(7):2459–66. https://doi.org/10.1007/s11664-014-3202-6.

[24] Long X, Hu B, Feng Y, Chang C, Li M. Correlation of microstructure and constitutive behaviour of sintered silver particles via nanoindentation. Int J Mech Sci 2019;161–162. https://doi.org/10.1016/j.ijmecsci.2019.105020.

[25] He G, Hongcheng W, Yao Y. Creep of sintered porous micron-silver: nanoindentation experiment and theoretical analysis. J Mater Sci 2021;56(32):18281–99. https://doi.org/10.1007/s10853-021-06426-8.

[26] Fan J, Jiang D, Zhang H, Hu D, Liu X, Fan X, Zhang G. High-temperature nanoindentation characterization of sintered nano-copper particles used in high power electronics packaging. Results Phys 2022;33. https://doi.org/10.1016/j.rinp.2021.105168.

[27] Chen H, Wang X, Zeng Z, Zhang G, Zhang J, Liu P. Solvent modulation, microstructure evaluation, process optimization, and nanoindentation analysis of micro-Cu@Ag core–shell sintering paste for power electronics packaging. J Mater Sci Mater Electron 2023;34(24). https://doi.org/10.1007/s10854-023-11083-5.

[28] Long X, Li Z, Lu X, Guo H, Chang C, Zhang Q, Zehri A, Ke W, Yao Y, Ye L, Liu J. Mechanical behaviour of sintered silver nanoparticles reinforced by SiC microparticles. Mater Sci Eng, A 2019;744:406–14. https://doi.org/10.1016/j.msea.2018.12.015.

[29] Okoro AM, Machaka R, Lephuthing SS, Oke SR, Awotunde MA, Olubambi PA. Nanoindentation studies of the mechanical behaviours of spark plasma sintered multiwall carbon nanotubes reinforced Ti6Al4V nanocomposites. Mater Sci Eng, A 2019;765. https://doi.org/10.1016/j.msea.2019.138320.

[30] Alao A-R, Yin L. Nanoindentation characterization of the elasticity, plasticity and machinability of zirconia. Mater Sci Eng, A 2015;628:181–7. https://doi.org/10.1016/j.msea.2015.01.051.

[31] Chen C, Suganuma K. Microstructure and mechanical properties of sintered Ag particles with flake and spherical shape from nano to micro size. Mater Des 2019;162:311–21. https://doi.org/10.1016/j.matdes.2018.11.062.

[32] Ishizaki T, Miura D, Kuno A, Hasegawa K, Usui M, Yamada Y. Young's modulus of a sintered Cu joint and its influence on thermal stress. Microelectron Reliab 2017;76–77:405–8. https://doi.org/10.1016/j.microrel.2017.06.015.

[33] Wang X, Yang Z, Wang B, Chen W, Zhang G, Zhang J, Fan J, Liu P. Effect of epoxy resin addition on properties and corrosion behavior of sintered joints in power modules serviced offshore. J Mater Res Technol 2023;25:6593–612. https://doi.org/10.1016/j.jmrt.2023.07.098.

[34] Romano Lapasin SP. Vittorio sirtori, donato casati viscoelastic properties of solder pastes. J Electron Mater 1998;27:138–48. https://doi.org/10.1007/s11664-998-0204-2.

[35] Oliver GMPWC. An improved technique for determining hardness and elastic modulus using load and displacement sensing indentation experiments. J Mater Res 1992;7:1564–83. https://doi.org/10.1557/jmr.1992.1564.

[36] Wang J, Yang C, Liu Y, Li Y, Xiong Y. Using nanoindentation to characterize the mechanical and creep properties of shale: load and loading strain rate effects. ACS Omega 2022;7(16):14317–31. https://doi.org/10.1021/acsomega.2c01190.

[37] Jiao ZM, Wang ZH, Wu RF, Qiao JW. Strain rate sensitivity of nanoindentation creep in an AlCoCrFeNi high-entropy alloy. Appl Phys A 2016;122(9). https://doi.org/10.1007/s00339-016-0339-6.

[38] Goodall R, Clyne TW. A critical appraisal of the extraction of creep parameters from nanoindentation data obtained at room temperature. Acta Mater 2006;54 (20):5489–99. https://doi.org/10.1016/j.actamat.2006.07.020.

[39] Zhao J, Huang P, Xu KW, Wang F, Lu TJ. Indentation size and loading strain rate dependent creep deformation of nanocrystalline Mo. Thin Solid Films 2018;653:365–70. https://doi.org/10.1016/j.tsf.2018.03.068.

[40] Huang P, Wang F, Xu M, Xu KW, Lu TJ. Dependence of strain rate sensitivity upon deformed microstructures in nanocrystalline Cu. Acta Mater 2010;58(15):5196–205. https://doi.org/10.1016/j.actamat.2010.05.055.

[41] Karuna Tunvisut NPOD, Busso Esteban P. Use of scaling functions to determine mechanical properties of thin coatings from microindentation tests. Int J Solid Struct 2001;38(2):335–51. https://doi.org/10.1016/S0020-7683(00)00017-2.

[42] Luo J, Lin J. A study on the determination of plastic properties of metals by instrumented indentation using two sharp indenters. Int J Solid Struct 2007;44 (18–19):5803–17. https://doi.org/10.1016/j.ijsolstr.2007.01.029.

[43] Zhuk DI, Isaenkova MG, Perlovich YA, Krymskaya OA. Finite element simulation of microindentation. Russ Metall 2017;2017(5):390–6. https://doi.org/10.1134/S0036029517050123.

[44] Cheng Y-T, Cheng C-M. Scaling, dimensional analysis, and indentation measurements. Mater Sci Eng R Rep 2004;44(4–5):91–149. https://doi.org/10.1016/j.mser.2004.05.001.

[45] Su W, Wei SS, Hu SQ, Tang JX. Preparation of TiO(2)/Ag colloids with ultraviolet resistance and antibacterial property using short chain polyethylene glycol. J Hazard Mater 2009;172(2–3):716–20. https://doi.org/10.1016/j.jhazmat.2009.07.056.

[46] Bhogaraju SK, Kotadia HR, Conti F, Mauser A, Rubenbauer T, Bruetting R, Schneider-Ramelow M, Elger G. Die-attach bonding with etched micro brass metal pigment flakes for high-power electronics packaging. ACS Appl Electron Mater 2021;3(10):4587–603. https://doi.org/10.1021/acsaelm.1c00721.

[47] Liu Z, Tang B, Zhang S. Properties of stable aqueous nanofluids composed of copper nanoaggregates for enhancing heat transfer. Ind Eng Chem Res 2022;61(4):1596–605. https://doi.org/10.1021/acs.iecr.1c04058.

[48] Fu S, Mei Y, Li X, Ning P, Lu G-Q. Parametric study on pressureless sintering of nanosilver paste to bond large-area (≥100 mm2) power chips at low temperatures for electronic packaging. J Electron Mater 2015;44(10):3973–84. https://doi.org/10.1007/s11664-015-3842-1.

[49] Wang F, Huang P, Xu KW. Time dependent plasticity at real nanoscale deformation. Appl Phys Lett 2007;90(16):161921. https://doi.org/10.1063/1.2730735.

[50] Ding ZY, Song YX, Ma Y, Huang XW, Zhang TH. Nanoindentation investigation on the size-dependent creep behavior in a Zr-Cu-Ag-Al bulk metallic glass. Metals 2019;9(5). https://doi.org/10.3390/met9050613.

[51] Gao Z, Song Y, Pan Z, Chen J, Ma Y. Nanoindentation investigation on the creep behavior of P92 steel weld joint after creep-fatigue loading. Int J Fatig 2020;134. https://doi.org/10.1016/j.ijfatigue.2020.105506.